Stanford Geothermal Program
Final Report
July 1990 - June 1996

Stanford Geothermal Program
Department of Petroleum Engineering
Stanford University
Stanford, CA 94305-2220
USA

Table of Contents

1. THE EFFECTS OF ADSORPTION ON VAPOR-DOMINATED GEOTHERMAL FIELDS

This work was conducted by Shubo Shang, Antonio Correa, John Hornbrook, Roland N. Horne and Henry J. Ramey, Jr.

1.1 SUMMARY

Adsorbed water on the rock surfaces in vapor-dominated geothermal fields has long been thought to provide a major source of fluid within the reservoir. Over the past several years, the Stanford Geothermal Program has conducted a series of investigations into the phenomena of water adsorption in geothermal systems, and their effects on reservoir performance. The results and conclusions of the most recent studies will be summarized here.

The studies include: (1) an experimental investigation in which measurements of the adsorption and desorption isotherms on actual geothermal cores were made, including a study of adsorption characteristics in The Geysers field in California; (2) a theoretical investigation into how adsorption relates to capillary condensation, and how the combined phenomenon can be expected to act; (3) a theoretical, numerical and data investigation into how adsorption and desorption will affect reinjection at The Geysers field, including a study of adsorption effects evident in tritium tracer observations.

It has been found through these studies that the amount of (liquid) water adsorbed in vapor-dominated geothermal fields is very considerable, even at pressures well below the boiling point pressure. Adsorbed water represents the major fraction of fluid stored in the reservoir and can be the most important source. Reservoir performance forecasts are strongly governed by the amount, and the rate of release of adsorbed water. Adsorption seems only modestly affected by the presence of noncondensible gases. During reinjection, water adsorbs more easily than it subsequently is able to desorb, which results in a reduction in the efficacy of reinjection.

1.2 INTRODUCTION

In simple terms, a vapor-dominated geothermal reservoir consists of porous or fractured rock, with the interstitial spaces filled with steam. However, a more complete understanding of the behavior of this type of reservoir requires a more sophisticated description than this. Due to the processes of adsorption and capillary condensation, water molecules are stored on the surfaces of the pore

spaces in a state that is more like that of a liquid than that of a vapor. This is true even if the thermodynamic conditions are such that liquid water could not exist in a free space. The consequence of the adsorption phenomenon is that water exists in the pore space of a vapor-dominated geothermal reservoir, even though the steam present in large fractures and voids may be superheated. The large surface area of a porous material and the large density difference between the liquid and vapor states of water mean that the mass of liquid constitutes the major component of fluid storage, even though it is only vapor that flows to the wells.

The performance of a vapor-dominated geothermal reservoir is governed strongly by the effects of adsorption. The liquid phase represents most of the fluid in the reservoir, and sustains production beyond what might be expected for a reservoir filled only with vapor. While this is a very beneficial effect, adsorption complicates the analysis of the reservoir since the liquid water is "invisible" to the reservoir engineer. The useful life and sustainable production capacity of the reservoir is dependent on the quantity of adsorbed water in place, yet this quantity can be measured only indirectly. Furthermore, the effectiveness of reinjection into a vapor-dominated reservoir is also governed by the influence of adsorption. Hence, proper design and implementation of a reinjection scheme must take proper account of the adsorption phenomena.

Over the past several years, the Stanford Geothermal Program has conducted a number of investigations into the properties of adsorption and its effect on geothermal production and injection. The results of these studies will be summarized in the following sections. Separate issues to be discussed are: (1) What is adsorption? (2) How much adsorption occurs in geothermal reservoirs? (3) What are the properties of adsorbed water in geothermal rocks? (4) How does adsorption affect production and injection?

1.3 WHAT IS ADSORPTION?

Physical adsorption is caused mainly by Van der Waals attractive forces, including the dispersion force. In addition, there will be electrostatic forces if either the adsorbent or the adsorbate is polar in nature. The process is similar to condensation of vapor molecules onto a liquid phase of the same composition. The major characteristics of physical adsorption can be summarized as follows (Satterfield, 1980; Ruthven, 1984):

1. Physical adsorption is an exothermic process so the amount of gas physically adsorbed at constant pressure always decreases monotonically as temperature is increased. The average heat of physical adsorption for the formation of a monolayer usually exceeds that of liquefaction, but seldom by more than a factor of about two.

2. Physical adsorption requires no activation energy and therefore can occur nearly as fast as molecules strike a surface. The process is reversible and equilibrium is established very rapidly unless diffusion through a fine porous structure limits the process.

3. Adsorption/desorption hysteresis is caused by geometric effects in that the specific curvature in contact with the vapor at a specified relative pressure (p/p_0) as vapor pressure is increased is different from that as the vapor pressure is decreased.

In a porous material, adsorption and capillary condensation are two closely related processes, i.e. they both cause the vapor to condense onto the solid. They are related in such a way that adsorption provides a precursor for capillary condensation. The physical processes of adsorption in porous materials can be divided into three steps: (1) submonolayer adsorption, (2) multilayer adsorption with transition to (3) capillary condensation. The pressure range at which the transition from multilayer adsorption to capillary condensation occurs depends on the structure of the material. If the material is microporous, the pore space will be filled up (commonly termed as volume filling) before multilayer adsorption is developed. In larger pores, multilayers of adsorbed water form as pressure increases. At a certain pressure, capillary condensation commences in the small pores. As the pressure is progressively increased, wider and wider pores are filled while multilayer adsorption is simultaneously taking place.

1.4 ADSORPTION IN GEOTHERMAL RESERVOIRS

In vapor-dominated geothermal systems, it has been proposed that liquid might exist as adsorbed liquid in micropores (White, 1973). Evidence from both laboratory studies (Hsieh, 1980, Herkelrath et al., 1983) and field data indicates that storage of liquid as micropore fluid is likely (Ramey, 1990). If it is assumed that the only mechanism for liquid storage is adsorbed water, then the desorption curve provides important information for performance matching and production forecasting. It is obvious that measurement of adsorption/desorption of water vapor on reservoir rocks is a crucial step in determining whether adsorption is the storage mechanism for these systems, and if so, what would be the appropriate procedure for performance prediction of vapor dominated geothermal systems.

Reservoir related water adsorption studies have been limited, especially at high temperatures. Hsieh (1980) constructed a BET (Brunauer, Emmett, and Teller) type of apparatus for high-temperature adsorption measurements. Hsieh (1980) conducted a number of adsorption measurements on Berea sandstone and unconsolidated silica sand. It was concluded that the characteristic adsorption curves for consolidated cores are temperature invariant and that adsorbed water may be an important source of steam in vapor-dominated geothermal reservoirs (Hsieh and Ramey, 1983). Luetkehans (1988) continued Hsieh's work by improving the apparatus.

Measurements of water adsorption isotherms were made on Berea sandstone, cores from The Geysers, California, and from Larderello, Italy. However, the true magnitude of the amount adsorbed was in question due to difficulties in establishing equilibrium. In addition, the long equilibrium time required made the leakage of high-temperature valves a significant factor in causing experimental error. Laboratory studies of water adsorption in porous media were also conducted by Herkelrath and his coworkers in association with their work on steam flow in porous media (Herkelrath et al., 1983) and the disposal of nuclear waste (Herkelrath and O'Neal, 1985). They reported a higher level of adsorption, but otherwise findings similar to those of Hsieh and Ramey (1983).

Clearly, there was a need to improve on the apparatus for water adsorption tests on geothermal rocks at high temperatures. It was appealing to automate the adsorption experiments in the interest of both sparing the operator for other tasks and in reducing experimental error. Harr (1991) performed preliminary investigations on the use of an automated sorptometer from Porous Materials, Inc. (PMI) for high-temperature water adsorption measurements. To our knowledge, this is the first commercial sorptometer built for automated high-temperature adsorption tests. The results of this series of measurements has been described in Shang, Horne and Ramey (1994, 1995) and will be summarized here.

Adsorption of water vapor on Berea sandstone and The Geysers well NEGU-17 graywacke was carried out at temperatures of 80, 100, 120 and 130^{o}C. Fig. 1 shows the adsorption/desorption isotherms on the two samples at 120^{o}C. A comparison of this figure with similar measurements for Berea sandstone shows that the amount of water adsorbed at any given relative pressure is higher on Berea sandstone than on The Geysers graywacke. This is expected since Berea sandstone has a larger surface area. At relative pressures below 0.6, the amount of water adsorbed can be approximated by a linear function of relative pressure in both cases. However, the linear relationship breaks down as pressure increases and the amount of water adsorbed increases rapidly with pressure. This change in the shape of the adsorption isotherm is an indication that capillary condensation has taken place and its contribution to total water retention by the reservoir rock becomes increasingly more significant as pressure is further increased.

There is an obvious hysteresis and it persists to very low pressure. Detailed discussion on the occurrence and possible causes of the observed hysteresis for water adsorption/desorption is presented in Shang, Horne and Ramey (1994a).

Fig. 2 shows the variation of adsorption with temperature in a core from The Geysers. Comparison of Figs. 1 and 2 reveals that the overall quantity adsorbed varies from one part of the

field to another. The same observation was made comparing measurements from reservoir samples from Italy.

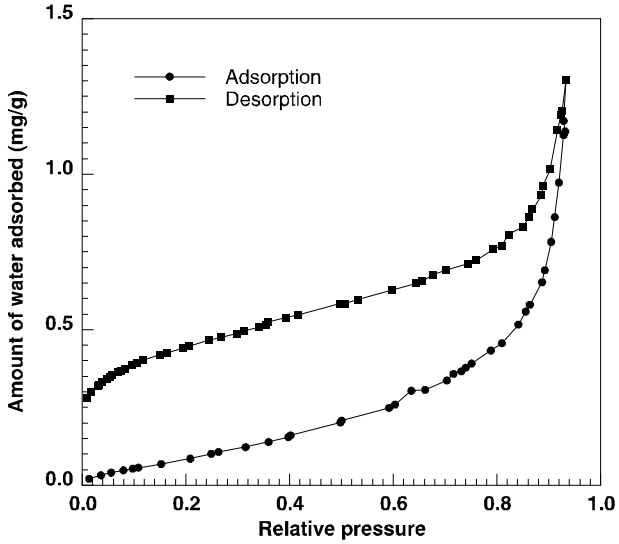

Figure 1: Water Adsorption/Desorption Isotherms for Geysers NEGU-17 Graywacke at 120^{o}C

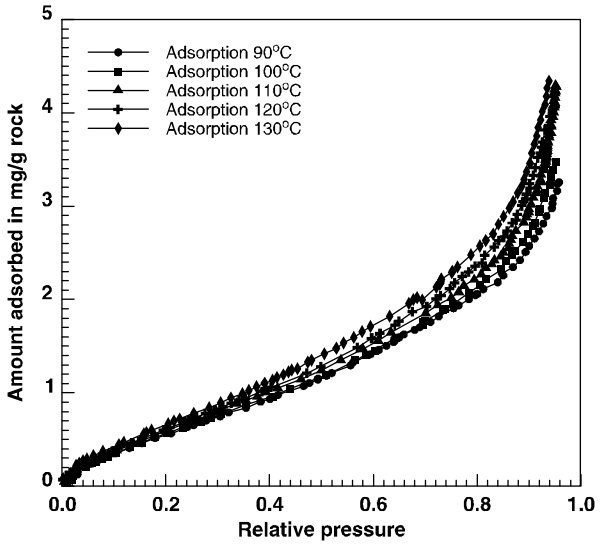

Figure 2: Adsorption Isotherms on Geysers MLM-3 Sample at Different Temperatures

Adsorption isotherms, such as those shown in Figs.1 and 2, are often shown as mass adsorbed per mass of rock. It is useful to look at the mass adsorbed in terms of liquid saturation, by converting the mass adsorbed per mass of rock (X) using the following equation:

$$S_w = \frac{1-\phi}{\phi}\frac{\rho_r}{\rho_w} X \qquad (1)$$

Making the conversion to water saturation reveals that adsorption accounts for a large volume of liquid water, as shown in Fig. 3 (which is a conversion of one of the isotherms from Fig2).

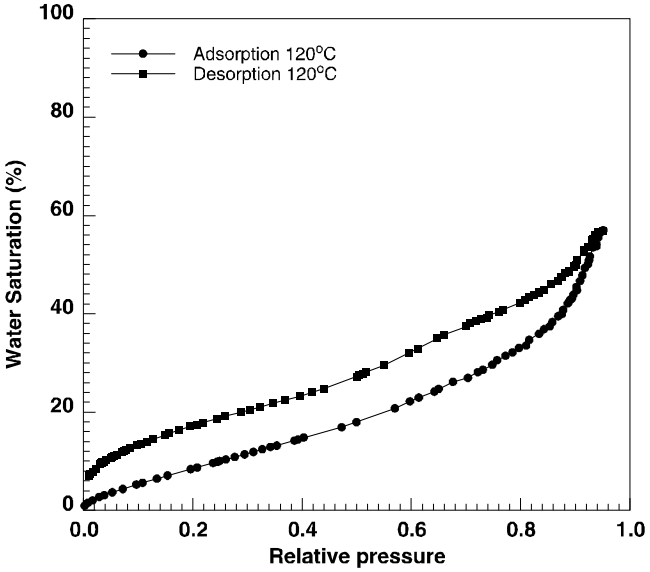

Figure 3: Adsorption Isotherms for Geysers MLM-3 Sample, Plotted as Saturation.

Based on these measurements, it can be concluded that a major fraction of the pore space in a vapor-dominated geothermal reservoir is filled with liquid water, even at pressure significantly below the saturation pressure.

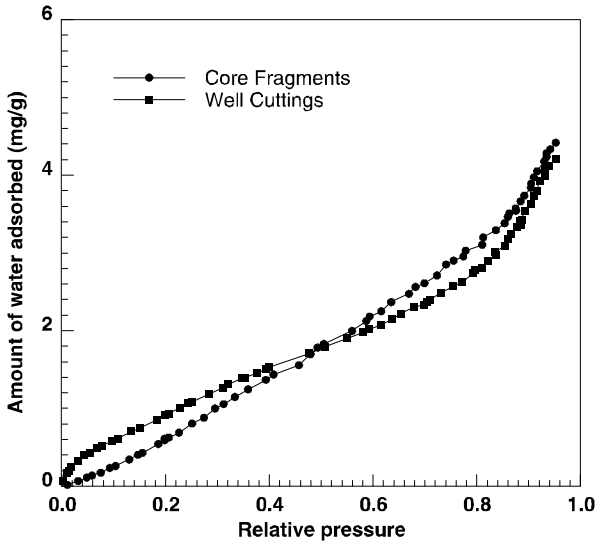

Figure 4: Comparison of Adsorption Isotherms on Core and Well Cuttings

An important result from Shang, Horne and Ramey (1994) was that measurements of adsorption made using cores were effectively the same as those made using cuttings from the same well. Since cores are usually difficult and expensive to obtain, this means that adsorption measurements can be made over a wide range of reservoir locations. Fig.4 shows a comparison of adsorption measurements made on cuttings from a Geysers well, compared to measurements made on a core from the same well.

1.5 PROPERTIES OF ADSORPTION

Correa and Ramey (1994) conducted an investigation into the theoretical aspects of adsorption in a porous medium. They discussed the conditions under which adsorption and capillary condensation occur, and developed equations to estimate the magnitude of the effects. From the point of view of geothermal reservoirs, pure adsorption is an effect that takes place at low pressure whereas capillary condensation occurs at pressures close to the saturation pressure. At intermediate pressures, the "adsorption" phenomenon is a combination of both physical adsorption and capillary condensation, and for the purposes of discussion of reservoir performance there is no real need to distinguish between the two effects. Important in the discussion of Correa and Ramey (1994) is the concept of a critical radius r_c, which is equivalent to the radius of space spanned by a steam molecule, r_g, at a given temperature and pressure. If a pore is smaller than r_g, then it is impossible for a vapor molecule to enter, and capillary condensation cannot take place. This places a lower limit on the occurrence of capillary condensation. The combined effects of adsorption and capillary condensation can be seen in an estimated isotherm in Fig5. It should be noted that the effect of the critical radius is to reverse the trend of adsorption with temperature so that the amount adsorbed increases with temperature at a given relative pressure, which is as measured in The Geysers core samples.

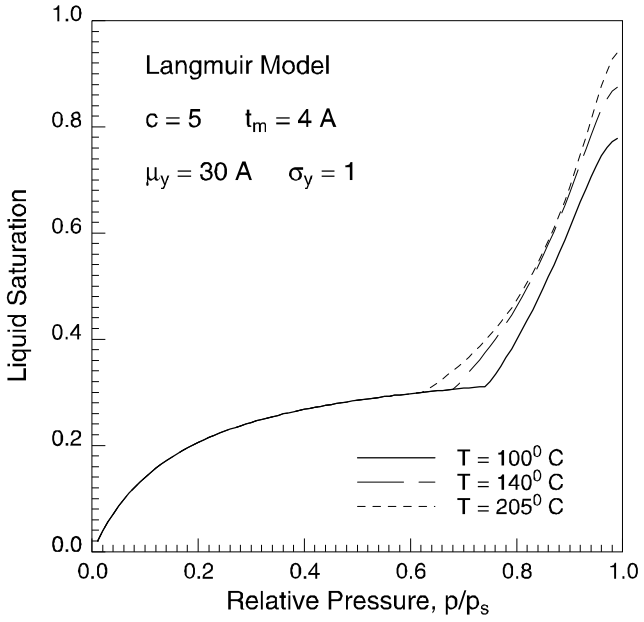

Figure 5: Theoretical Adsorption and Capillary Condensation Isotherms.

Another aspect of adsorption that required investigation was the physical properties of the adsorbed phase. Hornbrook (1994) examined density, enthalpy and heat of desorption of the adsorbed water phase. Although these properties vary somewhat from those of liquid water, Hornbrook (1994) concluded that, from the point of view of modeling geothermal reservoirs, it was acceptable to use the properties of saturated liquid water.

1.6 EFFECTS ON PRODUCTION AND INJECTION

The effects of adsorption on geothermal reservoir performance have been discussed by Economides and Miller (1985), Ramey (1990) and Hornbrook (1994). The fundamental influence of the presence of the adsorbed phase is to support the reservoir pressure to a much larger extent than would be expected with steam alone. An example of the pressure decline in a hypothetical reservoir model with varying degrees of adsorption is shown in Figs 6 and 7 from Hornbrook (1994).

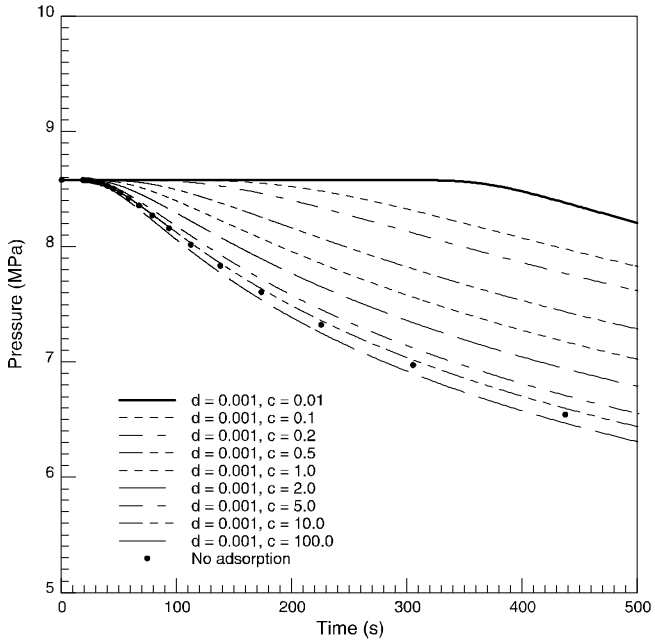

Figure 6: Early Time Depletion Effects with Adsorption.

The parameters *d* and *c* in Figs. 6 and 7 represent the magnitude of the adsorption and the curvature of the isotherm in a Langmuir type behavior, as described by a modified form of the Langmuir equation:

$$X = d\left[\frac{c(p/p_0)}{1+(c-1)(p/p_0)}\right] \tag{2}$$

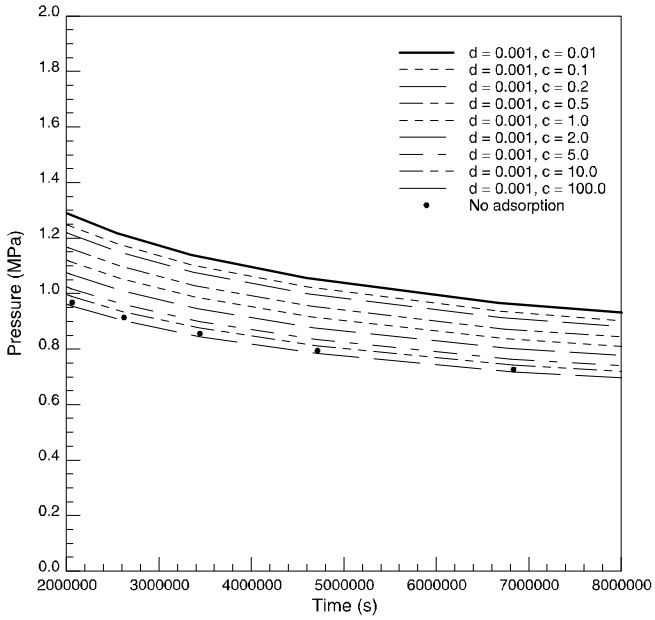

Figure 7: Late Time Depletion Effects with Adsorption.

In model calculations using measured Geysers isotherms such as the one shown earlier in Fig. 2, Hornbrook (1994) found behavior qualitatively similar to calculations using the Langmuir isotherm with *c* values less than 1.0 (concave upward isotherms).

The effects of adsorption on geothermal reservoir production can be estimated using a simulator that accommodates the adsorption phenomenon, provided that the form of the adsorption isotherm for the reservoir formation has been measured or inferred.

The effects of adsorption on injection can be estimated using similar concepts, however it is no longer clear that adsorption is beneficial. If injection results in a local increase in pressure in the vicinity of the injection well, then the quantity of water adsorbed must increase in a manner similar to that shown in Fig. 2. This means that injected water adds to local storage of liquid in the reservoir, rather than to general production of steam. This additional stored liquid will eventually desorb as pressures decline, however this may be a long term effect that diminishes the near-term benefits of injection. For example, during the Low Pressure Area (LPA) injection test in The Geysers in 1991, Enedy, Enedy and Maney (1992) reported that 9.1×10^8 kg of water were injected over an area of about 3.2×10^6 m^2, resulting in a pressure increase from 1.03 MPa to 1.31 MPa. Based on Geysers adsorption measurement such as those in Fig. 2, Hornbrook (1994) estimated that about 5.2×10^8 kg of water were readsorbed, or about 57% of the total amount injected. Evaluation of the effectiveness of an injection scheme therefore needs to address the counteracting influences -- raising pressures will result in higher productivity in the production wells, but will cause less injected fluid to be immediately available as steam.

1.7 CONCLUSIONS

Reservoir engineering design of production and reinjection schemes in vapor-dominated geothermal reservoirs must take proper account of the effects of adsorption. The general effect of adsorption is to support production. To estimate the extent of this support, it is necessary to make measurements of the adsorption isotherms of the particular reservoir rocks. Fortunately, it has been determined that these measurements can be made using well cuttings instead of cores. Theoretical studies indicate that adsorption should increase with temperature at a given relative pressure; this conclusion was confirmed in laboratory measurements.

Based on the measured adsorption isotherms for The Geysers geothermal field, allowing reservoir pressure to rise during reinjection may result in substantial short-term reduction in effectiveness of injection. The overall efficiency of an injection scheme needs to take this into account.

2. ADSORPTION CHARACTERISTICS OF ROCKS FROM VAPOR-DOMINATED GEOTHERMAL RESERVOIR AT THE GEYSERS, CA

This work was conducted by Cengiz Satik, Mark Walters and Roland N. Horne

2.1 SUMMARY

This section reports on a continuing experimental effort to characterize the adsorption behavior of rocks from The Geysers steam field in California. We show adsorption results obtained for 36 rock samples. All of the adsorption isotherms plotted on the same graph exhibit an *envelope* of isotherms. The minimum and the maximum values of the slope (or rate of adsorption) and of the magnitude within this *envelope* of isotherms belonged to the UOC-1 (felsite) and NCPA B-5 (serpentine) samples. The values of surface area and porosity, and pore size distribution for 19 of the samples indicated a very weak correlation with adsorption. An interpretation of the pore size distributions and the liquid saturation isotherms suggests that the change in the slope and the magnitude of the adsorption isotherms within the *envelope* is controlled primarily by the physical adsorption mechanism instead of capillary condensation. Grain-size and framework grain to matrix ratio are found to be insufficient to characterize this adsorption behavior. An accurate identification of the mineralogy of the samples will be essential to complete this analysis.

2.2 INTRODUCTION

In general, geothermal systems can be categorized as liquid- or vapor-dominated reservoirs depending on liquid water saturation level. In liquid-dominated systems, the resident fluid is mostly hot liquid water while it is mostly saturated or superheated steam in vapor-dominated systems. Vapor-dominated systems are the most attractive commercially because of their high energy content. Examples of such systems are Larderello, Italy and The Geysers, CA. The focus of this study has been on The Geysers geothermal field in California.

In an early attempt to explain the source of The Geysers geothermal reservoir, White (1973) suggested that liquid might either be supplied from an external water aquifer or exist at an adsorbed state in pore space. Since further research has failed to prove any evidence of such an external water source, the phenomena of adsorption is the more likely mechanism. If this is the case, then it is very important to identify and to measure the quantity of so called “adsorbed water” in the reservoir in order to forecast correctly the production capacity and the life of the reservoir. Moreover, the effects of this phenomenon must be accounted for when designing a proper

reinjection/production process in The Geysers since both fluid transport and storage will depend on how strong such effects are.

Although the fundamentals of the adsorption phenomena has long been well known and the body of the literature on the subject of adsorption at low temperature is large, the studies regarding adsorption at high temperatures are limited. Previously, a number of experimental and theoretical attempts were made at Stanford in order to measure the amount of adsorbed water and to improve the understanding of the adsorption behavior at The Geysers field. In 1980, Hsieh constructed a *BET* (Brunauer, Emmett and Teller) type of sorptometer and conducted adsorption experiments with Berea sandstone core and unconsolidated silica sand. His results showed that adsorption behavior is affected by temperature and that steam adsorption is a possible water storage mechanism (Hsieh and Ramey, 1983). Later, Luetkehans (1988) improved this equipment and conducted more experiments with Berea sandstone as well as with geothermal rock samples. Due to the excessive leaks that occurred during the long equilibrium times required when using core samples with very low porosity and permeability, the accuracy of these results were questioned. This problem was also encountered by Herkelrath et al. (1983) and Herkelrath and O'Neal (1985) in the studies of steam flow in porous media and nuclear waste disposal. Previous studies indicated the need for a better apparatus that could provide a better control of experimental errors.

After the acquisition of an improved, computer automated, high temperature adsorption equipment, Harr (1991) and Shang at al. (1994, 1995) reported a number of preliminary adsorption measurements on tight rock samples. Additional experimental results for the rock samples from The Geysers field were reported recently by Satik and Horne (1995). A comparison of the results obtained at 80, 100 and 120 ^{o}C showed that the effect of temperature is negligible on the adsorption cycle whereas it is of significance during the desorption. The results of Satik and Horne (1995) also revealed another interesting feature. Adsorption behavior for a few samples randomly selected at the various locations in The Geysers showed a possible adsorption *envelope* ranging from a low-valued curvilinear to a large-valued linear type of isotherms. The cause of these changes in the adsorption behavior was unclear. These results indicated the need for further research to understand and to characterize this behavior, which then led us to a more detailed and systematic study. The ultimate goals of this project are to ascertain if a correlation exists between adsorption behavior and intrinsic chemical and physical properties such as mineralogy, permeability and porosity, and to conduct an *adsorption survey* of the Geysers field if such a correlation exists.

In this section we discuss the continuing experimental effort towards this final goal. First, we discuss the general geologic condition at The Geysers and describe the main rock types. Next, we shall explain the methodology followed during the process of sample selection. Following this, we

give a brief description of the experimental apparatus and procedure. Finally, we discuss the results of the adsorption experiments conducted for The Geysers samples selected for this study.

2.3 GEOLOGIC SETTING OF CORES

General Geologic Condition at The Geysers

The Franciscan Assemblage in the vicinity of The Geysers is well-known and described in numerous publications in detail that will not be repeated here (e.g.: Bailey et al., 1964; McLaughlin and Donnelly (editors), 1981; GRC Special Report 17, 1992). At The Geysers, the Franciscan Assemblage occurs as a sequence of tabular, stratigraphically continuous, slabs bounded by thrust faults known to some as "thrust packets" which dip eastward (Thompson, 1992). These were intruded by a composite, shallow, granitic Quaternary pluton of batholithic proportions thought to underlie an area of approximately 40 to 50 square miles beneath The Geysers

A large portion of The Geysers geothermal reservoir is within a thick, areally extensive body of metamorphic, graywacke sandstone. This body of metagraywacke can be subdivided into turbidite deposits of deep water submarine fans. In the Central portion of The Geysers, the metagraywacke section is often composed of massive, medium to coarse-grained proximal sandstone turbidites. In the Northwest Geysers, the metagraywacke units become thinner and finer grained, with intervals of siltstone and argillite interbeds, and other stratigraphic features characteristic of distal turbidite sequences (Sternfeld, 1989). The metagraywacke reservoir is interrupted by tectonically mixed units of rocks known as "melange" in the Northwest Geysers, and greenstone in the Southeast Geysers. The vast majority of steam entries in Geysers wells, however, occur in metagraywacke.

In the Central and Southeast Geysers, ophiolitic sequences of Franciscan greenstone, chert and serpentinized peridotite are the thrust packets which outcrop and form the caprock to much of reservoir. In portions of the Northwest Geysers. However, metagraywacke both outcrops and forms the entire geothermal reservoir section; the difference being that the metagraywacke "caprock" does not have an open fracture system, and the reservoir graywacke does. In the Northwest Geysers, the metagraywacke section above the pluton is believed to be at least 11,000 feet' thick. In the Southeast Geysers where the pluton is shallowest (now at -500 feet subsea elevation), the overlying metagraywacke section is as thin as 3500 feet thick. Here, the pluton was intruded sufficiently shallow into the crust so that the fracture system caused by the pluton reached the surface causing venting, decompression, boiling and convection (Walters et al., 1988).

Felsite

The term "felsite" is a general term applied to light-colored igneous rocks, and used locally to designate a large, granitic intrusive complex of batholithic proportions which is known to underlie The Geysers. An extensive study on this pluton has been reported in Hulen and Walters (1994).

The three major rock phases recognized by Hulen and Walters (1994) to underlie the Central and Southeast Geysers are: hornblende-pyroxene-biotite *granodiorite*, leucocratic biotite microgranite *porphyry* and orthopyroxene-biotite *granite*. The shallowest major felsite phase is rhyolite porphyry. Orthopyroxene-biotite granite dominates the top of the felsite in the Central Geysers. This granite is apparently a high-silica (77%) variety, though its composition has clearly been modified in part by hydrothermal alteration. Apparently the youngest and certainly the most mafic of the three major felsite phases is a distinctive, dark-colored granodiorite occurring at depth in the eastern portion of The Geysers. A core from this intrusive phase contains 67% SiO_2; thus it appears chemically to be a true granodiorite.

The intrusion of the felsite may have created both the vertical and horizontal fracture permeability and the basic "plumbing" needed to integrate pre-existing fractures remaining from the Jurassic-Cretacous subduction, Tertiary uplift and Quaternary tectonism of the San Andreas Fault Zone. As discussed by Sternfeld (1989), there is a strong correlation between occurrences of five major steam anomalies delineated by Thomas (1981) and the shallowest occurrences of steam underlain by the shallowest known occurrences of the felsite (Hebein, 1986). Many of the larger wells are also in close proximity to the drilled apices of the felsite.

The Geysers felsite is the basement rock in the Southeast and Central portions of The Geysers geothermal reservoir and is also the probable "basement rock" in the Northwest. More than 60 deep geothermal wells have penetrated the felsite. The overlying metagraywacke is thermally metamorphosed to a distance of 1000 feet to 2500 feet by the felsite throughout The Geysers (Walters et al., 1988; Sternfeld, 1989). The drilling data indicate that the thickness of The Geysers felsite may exceed 10,000 feet.

Metagraywacke

The reservoir rock at The Geysers is often called "graywacke", or the "main graywacke"; however this name belies the fact that the reservoir rock is primarily metagraywacke and has lost the petrophysical values associated with sedimentary sandstone. Previous analysis of cores from The Geysers reservoir show that the graywacke sandstone and intercalated shale have been metamorphosed to metagraywacke and argillite; that intergranular porosity has been reduced to almost nil; and that measurable porosity and permeability is in microfractures, along welded grain contacts, and in dissolution pores.

The Geysers "graywacke" is, in fact, a pumpellyite-grade metagraywacke with a weak and localized textural fabric (Type 1+) described by Blakeet al. (1967), and McLaughlin (1981). Although the textural and mineralogic grade of the metagraywacke is "weak" by petrographic standards, the metamorphism has had a significant effect on the porosity and permeability of the original graywacke sandstone. The Geysers "graywacke" should be classified as metagraywacke for petrophysical purposes after the usage of Hulenet al. (1991) when discussing its reservoir properties.

Graywacke is a subclass of sandstone. It consists of sand grains of quartz, feldspar and rock fragments embedded in a well-indurated dark gray to black clayey matrix. Matrix percentages greater than 15% are common and often exceed 50% of the total rock. Graywacke is composed of two components: framework grains and matrix material interstitial to the framework grains.

Framework grains range widely in size, from pebble to sand to silt particles (64mm to 0.01mm), and in composition. They are primarily quartz and feldspar with trace to minor accessory minerals such as epidote and biotite. Polymineralic rock fragments include greenstone, argillite, and chert. Most detrital grains are subangular to subrounded in shape.

Graywacke matrix is not a homogeneous monomineralic cement. It is an extremely inhomogeneous paste composed of many constituents. The most common are: silt-sized framework grains; incompetent lithic fragments such as greenstone which have been crushed and squeezed between competent framework grains; silica cement; and phyllosililcates cements including illite, montmorillonite, sericite and chlorite.

A fundamental aspect of the framework grain to matrix ratio is that the proportion of the matrix material increases as the size of the framework grains decreases. Thus, fine to very fine graywackes will appear more argillaceous because greater than 50% of the rockmay be composed of matrix paste. Coarse-grained graywackes, characterized by matrix percentagesof less than 20% will appear to be cherty or siliceous. In actuality, the matrixpaste is an admixture of clay cement and silica cement.It has a siliceous appearance because both silica and crystalline clay minerals are colorless at high magnification under a microscope.When the matrix material is primarily argillaceous, and the grains range from 0.01 to 0.05 mm, the rock is classified as argillite. Argillite is therefore an "end member" of the metagraywacke-argillite facies, as shale is an "end member" of the sandstone-shale facies.

2.4 METHODOLOGY

Sample Selection

The Geysers reservoir is a 3000 ft to 11000 ft thick section of Mesozoic metagrawacke with an area of about 50 sq.miles which has been intruded by a Quaternary granitic body of batholithic proportions locally known as "the felsite". More than 85% of the reservoir volume and steam resource are in the metagraywacke and granitic intrusive rocks, the remainder of the reservoir volume being intercalated units of metashale ("argillite"), metavolcanic greenstone, and serpentinite which have been tectonically mixed with the metagraywacke. The metagraywacke is derived from proximal and distal turbidite units which range from dark, fine-grained, argillaceous rock to light gray, coarse-grained litharenites. The essential difference between the metagraywacke subtypes is the grain size, and the amount of matrix paste which includes sericite (illite), chlorite, and smectite. A correlation between these lithologic differences in the metagraywacke the adsorption behavior is sought.

36 samples of core at 18 locations in the vapor-dominated reservoir at The Geysers were selected for adsorption measurements. These samples were selected to represent the variations in lithology across the reservoir so that the measurements can be used to define the adsorption properties of each significant rock type, and to determine if correlations with adsorption can be made with depth, geologic structure, and other physical properties including porosity, surface area, and pore structure.

Distribution of the samples selected for this study were as follows: thirteen silty to fine-grained, twelve medium-grained and five medium to coarse-grained, lithic metagraywacke samples of core were selected within metagraywacke. There are three units known within the felsite intrusive complex: a biotite granite being areally most extensive at the top of the pluton; a granodiorite apparently predominant at depth, having assimilated the biotite granite; and a rhyolite porphyry. One sample from each of these three felsite units were selected. Argillite is an end member of the graywacke-argillite facies in the same manner as shale is an end member of the sandstone-shale facies. One argillite sample of core was selected. Finally one sample of greenstone and one sample of serpentine were also included. The Geysers steam field is elongated along a NW-SE axis. The geographic distribution of the 36 samples is weighted toward the center of the field where the large number of wells are drilled: nine samples from Northwest Geysers, 19 samples from Central Geysers and eight samples from Southeast Geysers.

Experimental Apparatus and Procedure

Our experimental apparatus is a computer-automated, high temperature sorptometer (built by Porous Materials, Inc.). Details of the experimental apparatus and procedure were given in Satik and Horne (1995). Briefly, it consists of three isolated chambers (electronics, top and sample

chambers), a computer system and a vacuum pump. All of the electronics that control the operation are located inside the electronics chamber, which is kept at room temperature. The top chamber consists of a set of valves, transducers and thermocouples, a steam vessel, a heater and a fan. This chamber is kept at a temperature higher than the experiment temperature (currently up to 150°C). Finally, the third chamber is the sample chamber where a sample tube container is located. The sample chamber has a separate heating system such that it can be kept at the experiment temperature. A control software loaded in the computer system is used to operate and carry out sorption experiments.

Since the equipment is computer-automated, the experimental procedure is simple. Normally, an operator only needs to load the sample and start the control software. The remaining experimental procedure is carried out under computer control. Before each experiment, a new sample is outgassed under vacuum for 10-12 hrs. at 180 °C. Then, the procedure summarized in Satik and Horne (1995) is followed to obtain points on an adsorption or a desorption isotherm.

Due to the physical configuration of the sample cell (a steel U-tube with inner diameter of 9.65 mm), before starting each experiment, the rock (core) samples to be used are normally crushed into smaller pieces (particle size of 0.355 mm or larger). This procedure raises an important question regarding the sensitivity of the results to the particle sizes. Therefore, in order to address this point adsorption experiments have been carried out with crushed rock samples sieved at four different mesh ranges (particle sizes of up to 2 mm, 0.833-2 mm, 0.355-0.833 mm and 0.104-0.355mm). The adsorption curves obtained for the samples with particles of sizes of 0.355 or larger are similar while it differs significantly when the particle size are between 0.104 and 0.355 mm (Figure 8).

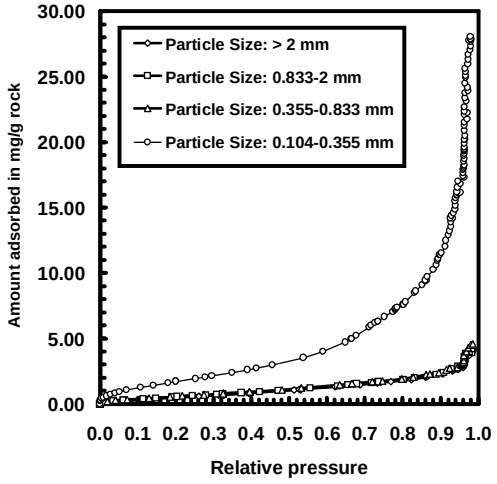

Figure 8: The effect of particle size on adsorption.

These results suggest that the use of crushed samples that contain particles of at least 0.355 mm large is appropriate to represent the overall adsorption behavior. Moreover, the adsorption equilibrium time could be extremely long for tight core samples, such as from The Geysers, with porosities of order of a few percent. Use of moderately crushed samples conveniently reduces the experiment run time and reduces the danger of leaks.

2.5 DISCUSSION OF RESULTS

Sorption experiments were carried out towards the final goal of conducting an *adsorption survey* of The Geysers geothermal field. 36 samples were selected by following the methodology outlined above. Although both adsorption and desorption isotherms have been obtained experimentally at 120 ^{o}C for all of The Geysers samples selected, we discuss only the adsorption isotherms in the scope of this work. Analysis of the desorption isotherms will be given in the future.

After the adsorption experiments were completed for all of the samples, measurements of surface area, porosity, pore size distribution and grain density were also performed on the same samples at a commercial laboratory. A summary of all of the results are given in Table 1. All of the sorption data obtained in our laboratory are currently accessible to the public through the Internet. Our World Wide Web page URL address is: http://ekofisk.stanford.edu/geoth/ads-data.html.

In Figure 9, the adsorption isotherms obtained from the sorption experiments for all of the 36 samples selected for this study are shown. The figure shows an *envelope* created by the end-point isotherms of UOC-1 and NCPA B-5 samples.

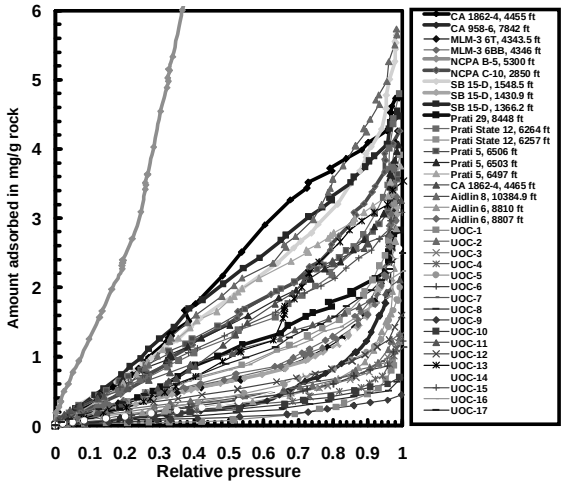

Figure 9: Results of the adsorption experiments for the 36 Geysers samples.

The slope and the magnitude of these isotherms within the *envelope* is the largest for NCPA B-5 and the smallest for UOC-1 while all of the other isotherms fall within these two curves. NCPA B-

5 is the only core sample of serpentine and its lithologic description (Table 1) is serpentine, serpenitized very fine-grained metagraywacke and silty-textured argillite, all of which are expected to have a very strong adsorptive behavior. On the other hand, UOC-1, leucocratic rhyolite porphyry (high silica granite), is one of the three felsite samples selected for this study.

Table 1: Summary of the results

	Elev. to Steam	Elev. to Felsite	ROCK	ADSORPTION at	ADSORPTION at	ADSORPTION,	ADSORPTION,	SURRFACE	POROSITY	DENSITY	LITHOLOGIC
CORE	from Core, ft	from Core, ft	TYPE	P/Po=0.5, mg/g	P/Po=0.75, mg/g	Langmuir Coef, c	Langmuir Coef, d	AREA, m^2/g	VOL. %	G/CM3	DESCRIPTION
AIDLIN 6	139	unknown	medium mgw	0.443442758	1.038067799	0.165176903	3.124115375	0.6704	3.33	2.7029	Med. gray, medium-grained, massive mgw
AIDLIN 6	142	unknown	medium mgw	0.125196726	0.350883131	0.030980009	4.103252109	0.39	5.03	2.736	Med. gray, medium-grained, massive mgw
AIDLIN 8	710	unknown	argillite	1.74369027	3.225969482	0.450203339	5.613147248	0.0709	2.28	2.8008	Dk. gray argillite
CA1862-4	-75	-3000	fine mgw	2.176996406	3.405932502	0.847721503	4.743964583	0.5374	3.26	2.8093	Dark gray, fine grained, gneissic metagraywacke
CA1862-4	-65	-3000	coarse mgw	1.242854467	2.093908941	0.642154185	3.17718897	0.3158	2.62	2.766	Dark gray, predominantly coarse grained, sl. foliated mgw.
CA958-6	2171	52	felsite	0.187645997	0.510575498	0.043602634	4.403777051	0.1339	3.59	2.7395	Dark, hornblende-pyroxene-biotite granodiorite.
MLM-3	-1735	-4270	fine mgw	0.287612052	0.769594919	0.062346583	4.817630776	0.7551	5.52	2.7507	Med. light gray, fine to medium grained metagraywacke
MLM-3	-1733	-4268	medium mgw	0.375962782	0.960486522	0.093051579	4.374406985	0.874	5.11	2.7466	Med. gray, med. grained metagraywacke.
NCPA B-5	500	-2600	serp.&serp. mgw	7.781898089	11.78075987	0.96399811	15.85415954	1.8689	5.74	2.8816	Serpentine & serpenitized v.f.-grained mgw and silty- textured argillite
NCPA C10	273	-4495	greenstone	1.378674198	2.4821875	0.500138242	4.135059559	0.9177	3.42	3.0126	Med. to dark green, hard, aphanitic greenstone.
P. S. 12	1479	-3700	fine mgw	0.955847335	1.670237934	0.555723471	2.670894211	0.7905	4.17	2.7616	Med. gray, fine grained metagraywacke
P. S. 12	1486	-3700	medium mgw	1.748698582	2.645198841	0.967043897	3.556955812	1.0626	4.49	2.7647	Med. greenish gray, medium grained metagraywacke.
PRATI 29	376	-3500	fine mgw	1.340453565	2.341782735	0.55981203	3.734000321	0.1554	2.65	2.7628	Dark gray, v.fine to fine grained metagraywacke.
PRATI 5	-438	-3500	fine mgw	1.503308544	2.368022468	0.823786149	3.32605298	0.8689	2.67	2.7544	Greenish black, very fine to fine grained metagraywacke.
PRATI 5	-432	-3500	fine mgw	0.525379192	1.215671264	0.164087756	3.671338731	1.46	2.87	2.7461	Med. greenish gray, fine to medium grained metagraywacke.
PRATI 5	-429	-3500	medium mgw	1.071462876	2.137912778	0.330153823	4.29616985	0.9862	3.04	2.7586	Med. dark gray, medium grained metagraywacke.
SB-15	-3	-3700	medium mgw	2.024311896	3.165671185	0.848605643	4.408681551	1.333	2.74	2.7473	Med. dark gray, medium grained, metagraywacke.
SB-15	62	-3700	fine mgw	1.5823974	2.984396318	0.414130715	5.385491689	3.1634	6.19	2.7346	Med. dark gray, fine grained, thin-bedded metagraywacke.
SB-15	179	-3500	coarse mgw	0.499556193	1.063516471	0.252433222	2.467831031	1.9125	3.59	2.7426	Med. gray, medium to coarse grained metagraywacke.
UOC-1	-587	435	felsite	0.07222295	0.195479	0.058568577	1.296102026				Leucocratic rhyolite porphyry (high-silica granite).
UOC-10	1549	-413	medium mgw	0.225531665	0.400805373	0.518354001	0.656901708				Med. lt. gray, medium grained metagraywacke.
UOC-11	1597	-3200	coarse mgw	1.076441945	1.54456015	1.201262936	1.973286566				Brownish gray, med.and med. to coarse grained lithic metagraywacke
UOC-12	1598	-3200	medium mgw	0.439153643	0.803996494	0.462512973	1.383283705				Lt. olive gray, medium grained metagraywacke
UOC-13	1601	-3200	fine mgw	1.112390192	2.082383431	0.429710264	3.695941755				Med. dark gray to brownish gray, fine grained mgw and metasiltstone
UOC-14	4560	1790	felsite	0.360572497	0.848939613	0.151280489	2.712817106				Orthophyroxene-biotite granite
UOC-15	678	-3137	fine mgw	1.335623304	2.098352712	0.833887208	2.936713927				Med. dark gray, fine to medium grained metagraywacke
UOC-16	686	-3129	fine mgw	0.78016668	1.34139546	0.593910362	2.093313588				Medium gray, fine grained metagraywacke
UOC-17	694	-3121	fine mgw	0.855964644	1.499180269	0.554071852	2.399520923				Med. gray, fine grained and dark gray v. fine grained metagraywacke
UOC-2	404	-2356	coarse mgw	0.350154005	0.659013619	0.407128002	1.196950307				Lt. to med.-lt. gray, med. to coarse grained metagraywacke
UOC-3	406	-2354	medium mgw	0.27368017	0.555552304	0.307956462	1.153453239				Lt. gray, medium grained metagraywacke
UOC-4	409	-2351	medium mgw	0.163969015	0.386676252	0.157435073	1.190794487				Lt. to med.-lt. gray, fine to medium grained metagraywacke
UOC-5	95	-1019	fine mgw	0.324665534	0.719791718	0.20836002	1.853467844				Dark gray to dk. greenish gray, v.fine grained metagraywacke.
UOC-6	97	-1017	coarse mgw	0.296036205	0.575503623	0.369636055	1.090154362				Light gray, coarse grained metagraywacke
UOC-7	99	-1015	medium mgw	0.359945996	0.637166946	0.516164962	1.048291888				Med. light gray, medium grained metagraywacke
UOC-8	1544	-418	medium mgw	0.166974857	0.328268873	0.351924842	0.637668515				Med. light gray, medium grained metagraywacke
UOC-9	1547	-415	fine mgw	0.115377768	0.224802036	0.362073405	0.430718122				Brn. black metasiltstone and grn. gray, fine to med. grained mgw

The adsorption isotherms given in Figure 9 include contributions from both surface (physical) adsorption and capillary condensation mechanisms of the adsorption phenomena. To analyze these results, some information about the contributions of each of the two mechanisms to the total amount adsorbed is needed. The first mechanism is related to the chemical and/or mineralogic composition of the rock while the second is mainly controlled by the topology of the rock (porosity, pore size distribution etc.).

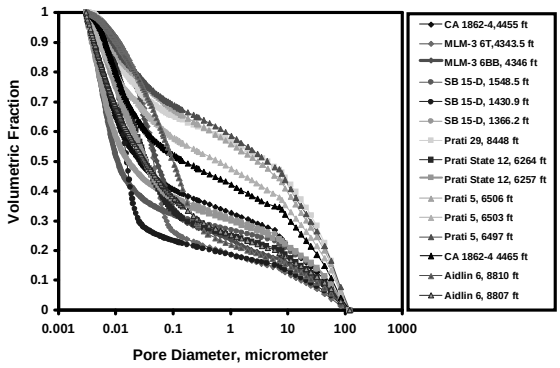

Figure 10: Pore size distributions for the 19 Geysers samples obtained from the mercury intrusion experiments.

Shown in Figure 10 are the volumetric fraction vs. pore diameter value curves for 19 samples, excluding all of the samples (surface area and porosity measurements on the samples are pending). These results were obtained from the equilibrated-step mercury intrusion experiments conducted at a commercial laboratory. In Figure10, the volumetric fraction denotes the ratio of the total mercury injected (in volume) at a pore diameter step to the total cumulative mercury injected (in volume) at the smallest pore diameter. The total cumulative volume of mercury injected at the smallest pore diameter is also the total pore volume within the rock detected by this method. The smallest value of the pore diameter obtained from these experiments is about 0.003 micrometer which requires a mercury pressure of as high as 60,000 psia.

In order to have a direct comparison, the rock samples used for adsorption measurements were also used for the mercury injection experiments. As discussed above, all of these rock samples were previously broken into smaller pieces (gravel-sized) before the adsorption experiments were conducted. However, we must note that the breaking process must have increased the external surface area, which in turn has increased the accessibility of pore space. Therefore, the total pore volume and the porosity values (see Table1) obtained from the mercury injection experiments should represent the absolute rather than the effective values. The effective values are expected to be somewhat smaller. Results shown in Figures9 and 10 are consistent. An *envelope* similar to that in Figure 9 is also apparent in Figure 10. Figure 10 shows that the lowest- and highest-end curves of the *envelope* belong to the samples from Sulphur Bank 15-D (1430.9 ft) and Prati 5 (6497 ft), respectively. The lowest-end curve reads a pore volume distribution as follows: 70% by the pores of sizes of 0.025 micrometer or less, 15% between 0.025 and 7 micrometer and 15% by the pores of sizes of 7 micrometer or larger. On the other hand, the pore volume distribution for the highest-end curve is as follows: 21% by the pores of sizes of 0.025 micrometer or less, 32% between 0.025 and 7 micrometer and 47% by the pores of sizes of 7 micrometer or larger.

In Figure 11, we show the liquid saturation vs. relative pressure curves obtained by using the adsorption isotherms given in Figure 9 and the total pore volume values obtained from the mercury injection experiments. From the figure, the final saturation values at the end of the adsorption cycle for Aidlin 6 (8810 ft) and NCPA B-5 (5300 ft are 0.147 (at p/p_o =0.98) and 0.662 (at p/p_o =0.995), respectively. The capillary condensation mechanism in pores are traditionally described by Kelvin's equation. Simply, this equation provides a relationship between a relative pressure and a characteristic radius (called Kelvin radius). At any capillary condensation stage, steam phase existing in all pores with a radius smaller than the Kelvin radius will be condensed through the capillary condensation mechanism. (Satik and Yortsos, 1995). For typical geothermal conditions, one can calculate a Kelvin radius value of 0.003 micrometer at p/p_o=0.91. The radius value of 0.003 micrometer is selected because it is the smallest pore radius detected by mercury injection experiments. At p/p_o=0.91, the liquid saturation values for the samples from Aidlin 6 (8810 ft) and NCPA B-5 (5300 ft) are 0.05 and 0.6, respectively (Figure 11). Therefore, adsorption process until at p/p_o=0.91 must take place only through the physical adsorption mechanism since the capillary condensation mechanism simply could not have started by the Kelvin equation. Interestingly enough, at this relative pressure value, %34 of the total adsorption has already taken place for Aidlin 6 (8810 ft) and %91 for NCPA B-5 (5300 ft). Therefore, we conclude that the rate of adsorption (the slope) for the isotherms shown in Figures 9 and 11 must be controlled only by the surface adsorption mechanism which depends mostly on the chemical/mineralogic composition of the rock.

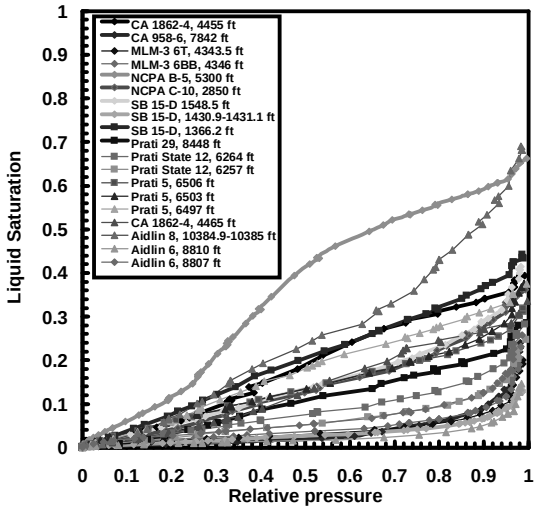

Figure 11: Liquid saturation vs. relative pressure curves obtained for the 19 Geysers samples.

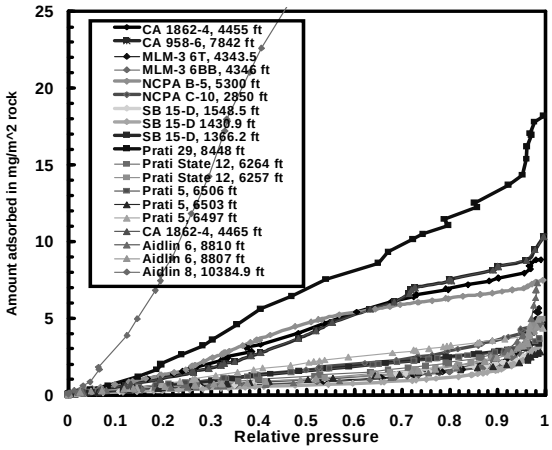

Figure 12: Surface area normalized adsorption isotherms for The Geysers samples.

Figure 12 shows adsorption isotherms normalized with surface area values for the 19 Geysers samples. An *envelope* similar to that in Figure 9 is also obtained which suggests that these changes observed in the adsorption behavior (the slope and the maximum adsorption value) are not caused by the surface area. However, surface area values for the remaining samples (for which measurements are still in progress) are required to fill in this *envelope.*

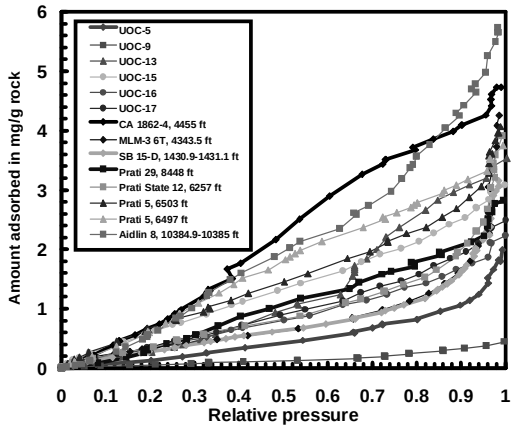

Figure 13: Adsorption isotherms for all of the fine grained-metagraywacke Geysers samples.

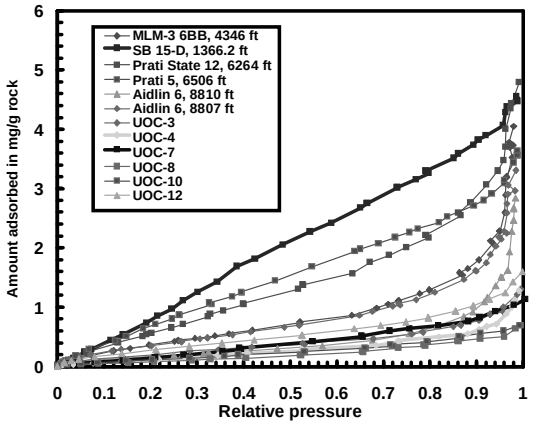

Figure 14: Adsorption isotherms for all of the medium grained-metagraywacke Geysers samples.

Figures 13, 14 and 15 show the adsorption isotherms obtained for the samples of fine-grained, medium-grained and coarse-grained metagraywacke subunits, respectively. A similar *envelope* with a large variation is seen also within the each subgroup of metagraywacke. The rate of adsorption (slope of isotherm) and the maximum adsorption value are expected to be higher for the fine to very fine grained-metagraywacke than for the medium or coarser grained-metagraywacke due to the fact that coarser samples have more grain than matrix material, therefore, they may contain less highly adsorptive minerals within the matrix. However, a comparison of the isotherms for the samples within the same subgroup shows that the grain size is apparently not a primary factor causing these changes. On the other hand, we believe that mineralogy may still be a key factor because samples from the different subunits of metagraywacke may actually have comparable amounts of highly adsorptive minerals (clays, micas etc.) although their matrix-grain ratio values are quite different from each other. Some of the most adsorptive metagraywacke samples in each subgroup are from the caprock, or near the top of the reservoir, SB 15-D is an example, and work by Hulen and Nielson (1995) shows that mixed-layer illite/smectite is a common vein mineral. This issue can be resolved by identifying the mineral contents for each Geysers sample and may be achieved by X-ray diffraction and/or thin-section analysis methods.

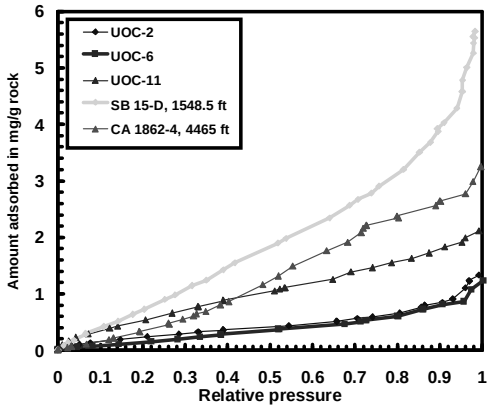

Figure 15: Adsorption isotherms for all of the coarse grained-metagraywacke Geysers samples.

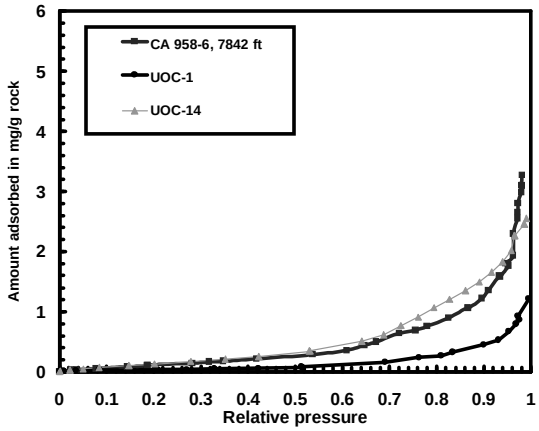

Figure 16: Adsorption isotherms for all of the felsite Geysers samples.

In Figure 16, we show the adsorption isotherms obtained from the experiments for the three felsite samples selected from The Geysers. Although we had only three samples from the felsite, these isotherms seem to agree well with each other and show an adsorption behavior similar to silicic metagraywacke. The felsite is predominantly plagioclase and quartz with relatively less mica/clay minerals (having a smaller rate of adsorption). However, considering the number of the felsite samples used, the agreement might well be coincidental. More adsorption experiments from the felsite are required to justify this.

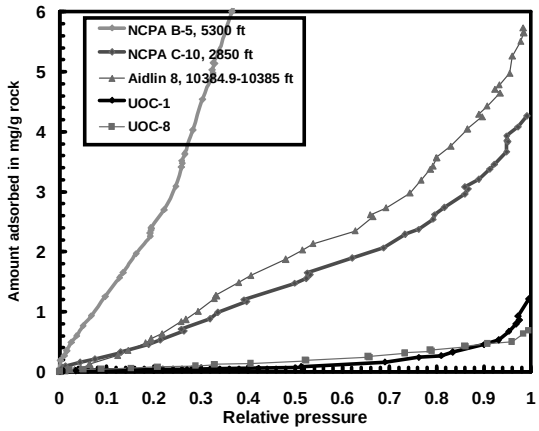

Figure 17: Adsorption isotherms for the samples representing each rock type in The Geysers. The rock types of serpentinite, argillite, greenstone, medium grained-metagraywacke and felsite are represented by the samples from NCPA B-5, Aidlin 8, NCPA C-10, UOC-8 and UOC-1, respectively

Finally, Figure 17 compares the adsorption isotherms for the samples from different rock types, namely serpentinite (NCPA B-5), argillite (Aidlin 8), greenstone (NCPA C-10), medium grained-metagraywacke (UOC-8) and felsite (UOC-1). As expected, the results show that the felsite (UOC-1) and serpentine (NCPA B-5) samples demonstrate the least and the strongest adsorption behavior, respectively, while the greenstone (NCPA C-10) and argillite (Aidlin 8) isotherms fall between them.

The total amount of water stored, and the rates of steam adsorption and condensation vary between the rock types and the subunits of the metagraywacke. Serpentinite appears to be the most adsorptive rock type and granitic felsite may be the least, with an order of magnitude difference between the two. The shapes of some adsorption curves together with mercury injection data suggest a bimodal porosity structure may exist in the metagraywacke.

Argillite and fine-grained metagraywacke have higher rates of adsorption for given pressures, and store several times the amount of water of the coarser grained metagraywacke and granitic felsite. The northwestern portion of The Geysers reservoir is characterized by thick sequences of distal turbidite units consisting of argillite and fine-grained metagraywacke. Consequently, the reservoir rocks of the Northwestern portion of The Geysers reservoir store more adsorbed water than the Central and Southeastern Geysers which is dominated by proximal turbidites units consisting of medium and coarse grained metagraywacke, and granitic felsite.

Greenstone and serpentinite constitute a small but significant portion of the reservoir section in the southeastern Geysers. Although the adsorption properties of the greenstone do not significantly differ from metagraywacke of the proximal turbidite units, the serpentinite found in some melange units is much more adsorptive. Consequently the lithologic details of any particular Geysers well may be important in characterizing the overall adsorptive properties of a particular portion of the reservoir.

2.6 CONCLUDING REMARKS

In this section, we have reported the results of adsorption experiments conducted for 36 Geysers samples. The adsorption results obtained for all of the samples exhibited an *envelope* of isotherms. The minimum and the maximum slope (or rate of adsorption) and absolute adsorption (the largest value attained) values within this *envelope* belonged to the isotherms of UOC-1 (felsite) and NCPA B-5 (serpentine) samples. Surface area, porosity and pore size distribution values for the 19 Geysers samples were measured at a commercial laboratory. Each of these measured values indicated only a very weak correlation with adsorption. Based on the pore size distributions and the liquid saturation isotherms, it was concluded that the change in the slope and the magnitude of the adsorption isotherms within the *envelope* is primarily controlled by the physical adsorption mechanism instead of capillary condensation. The adsorption isotherms for the metagraywacke samples indicate that the grain-size and framework grain to matrix ratio are insufficient measures to characterize this adsorption behavior. A more accurate identification of the adsorptive minerals is needed to complete the interpretation of the experimental results.

3. OPTIMIZING REINJECTION STRATEGY AT PALINPINON, PHILIPPINES BASED ON CHLORIDE DATA

This work was conducted by Ma. Elena G. Urbino and Roland N. Home

3.1 SUMMARY

One of the guidelines established for the safe and efficient management of the Palinpinon Geothermal Field is to adopt a production and well utilization strategy such that the rapid rate and magnitude of reinjection fluid returns leading to premature thermal breakthrough would be minimized. To help achieve this goal, sodium fluorescein and radioactive tracer tests have been conducted to determine the rate and extent of communication between the reinjection and producing sectors of the field. The first objective of this paper is to show how the results of these tests, together with information on field geometry and operating conditions were used in algorithms developed in Operations Research to allocate production and reinjection rates among the different Palinpinon wells.

Due to operational and economic constraints, such tracer tests were very limited in number and scope. This prevents obtaining information on the explicit interaction between each reinjection well and the producing wells. Hence, the chloride value of the producing well, was tested to determine if use of this parameter would enable identifying fast reinjection paths among different production/reinjection well pairs. The second aim, therefore, of this paper is to show the different methods of using the chloride data of the producing wells and the injection flow rates of the reinjection wells to provide a ranking of the pair of wells and, thereby, optimize the reinjection strategy of the field.

3.2 INTRODUCTION

The Palinpinon Geothermal Field is one of two producing steam fields currently operated by the Philippine National Oil Company (PNOC). The steam requirement of the 112.5 MWe commercial plant, known as Palinpinon 1 has been met by 21 production wells and 10 reinjection wells which accept wastewater by gravity flow. Figure18 shows the production and reinjection multiwell pads, as well as the well tracks. The need to reinject waste liquid effluent has been primarily dictated by environmental constraint, which in the Philippines prohibit full disposal into the rivers that are used for field irrigation. In addition to this, the other benefits of injection, such as maintaining reservoir pressures and increasing thermal recovery from rocks have been recognized.

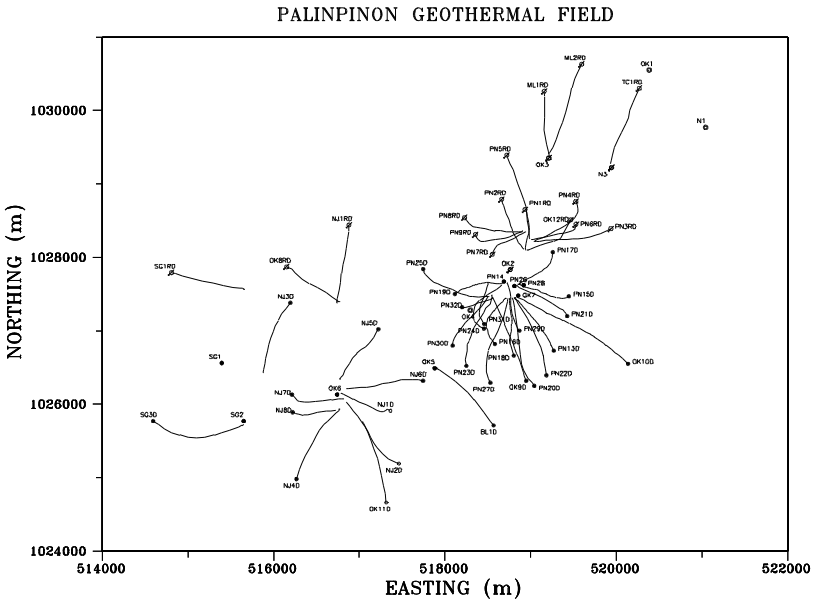

Figure 18: Palinpinon Geothermal Field

Although injection wells have been drilled at the periphery of the field, preferably at the identified outflows, initial chemical monitoring of the produced fluids showed increases in well reservoir chloride values. This has been interpreted as evidence of the return of reinjected fluids to the production sector. To maximize productivity of the reservoir and prolong the economic life of the field, guidelines for the safe and efficient management of the Palinpinon reservoir have been established. These include the requirements of:

1) Minimizing fluid residence times in the surface and downhole piping while operating reinjection wells to prevent or minimize silica deposition of injected fluid that is supersaturated with respect to amorphous silica.
2) Minimizing steam wastage due to varying steam demand and supply by prioritizing high enthalpy production wells during peak steam requirements and choosing injection wells with additional capacity.
3) Adopting a production and reinjection well utilization strategy such that the rapid rate and magnitude of reinjection fluids returns leading to premature thermal breakthrough would be minimized, if not avoided.

Towards this objective, a comprehensive testing and monitoring program was instituted. This program includes fluorescein and radioactive tracer testing to determine interaction between the injecting and producing blocks.

One aim of this work was to use the results of these tracer tests in algorithms of Operations Research to determine optimal production and reinjection rates among the different Palinpinon wells. However, since these tracer tests are limited, another objective was to find another parameter that could be used in place of tracer return data in the optimization of production and reinjection strategy.

3.3 TRACER TESTS AT THE PALINPINON GEOTHERMAL FIELD

Sodium fluorescein dye was injected into OK-12RD, PN-IRD, and PN-9PD while radioactive Iodine-131 was injected into OK-12RD and PN-9PD. Amounts of the dye and radioactive tracer were increased with succeeding tests to expand the scope of the tests and overcome the limitations imposed by degradation of the tracers.

The results show that the eastern injection wells (OK-12RD, PN-1RD, and PN-6RD) communicate strongly with the eastern and central Puhagan wells such as PN-15D, PN-17D, PN-21D, PN-26, PN-28, and OK-7. The western injection well PN-9RD, likewise, interact with the western, southwestern, and central Puhagan wells such as PN-14, PN-19D, OK-9D, PN-23, PN-24D, PN-29D, PN-30D, PN-31D, OK-7, PN-26, PN-28, PN-16D, and PN-18D. OK-7 had the earliest and strongest return during the PN-9PD tracer test. Coupled with interference testing and chemistry monitoring, results indicate fast interaction, too, of western injection wells PN-7RD and PN-8RD with the western and central Puhagan wells. Additional studies (PNOC-EDC, 1986) indicate that geological structures or faults are the preferred flow paths of the reinjected fluids back to the producing wells.

From radioactive tracer testing, one can obtain the tracer breakthrough time, the peak tracer recovery time, the peak tracer concentration, and the fraction of tracer recovered. This presents an advantage over fluorescein testing where only breakthrough times and the quality (intensity) of the return were established during the test. This is why only the results of the radioactive tracer test were used for the algorithms in the optimization study as discussed later.

Through this intensive chemical monitoring, tracer testing, as well as interference testing, injection and production wells with strong interactions have been identified; knowledge of which was employed to optimize the well utilization scheme. As an example, the northern and northeastern injection wells PN-2RD, PN-3RD, PN-4RD, and PN-5RD are considered "priority" in that they have exhibited minimal communications so far with the production wells. It is acknowledged that though almost all production wells produce reinjected fluid in varying proportions, the rate and magnitude of reinjection fluid returns are dependent on the combination of wells used for injection and production at any given time. It would be an advantage, therefore, to find a tool that would demonstrate or assess the interaction of a given injector/producer pair with time.

3.4 OPTIMIZATION STRATEGY

The results of the tracer tests, information on field geometry together with operating conditions were used to test algorithms from Operations Research to allocate reinjection and production rates in Palinpinon wells. These algorithms were modified by Lovekin (1987) to optimize injection scheduling in a geothermal field.

Essentially under this strategy, the reservoir is idealized as a network of channels or arcs connecting each pair of wells in the field. The arc cost, c_{ij}, expresses the likelihood of thermal breakthrough resulting from the movement of a unit fluid from injection i to producer j. It consists of weighting factors which are taken from tracer return data, field geometry and field operating conditions as shown by Equation(3).

$$c_{ij} = \frac{1}{t_i}\frac{1}{t_p} C_p f \frac{1}{L^2} e^{sh} \frac{q_p}{q_{pt}} \frac{1}{q_{rt}} \qquad (3)$$

where:

t_i = initial tracer response, days

t_p = peak tracer response, days

C_p = peak tracer concentration, t^{-1}

f = fractional tracer recovery

L = horizontal distance between wells, meters

h = elevation difference between production and injection zones, meters

s = scaling factor

q_p = producing rate under operating conditions

q_{rt} = injection rate during tracer testing

The results of the tracer tests demonstrate that the earlier the breakthrough or initial tracer response, the greater the tracer return, and the greater the likelihood for thermal breakthrough. Hence, the times of initial (t_i) and peak (t_p)tracer response are made to be inversely related to the arc cost c_{ij}. In contrast, the fraction of tracer recovered (f) and the peak tracer concentration (C_p) are made linear to the arc cost.

For a porous medium type of reservoir, the thermal recovery of injected fluid depends on the heat exchanged between the fluid and the rocks. Since this rock surface heat area is proportional to L^2, then the probability of thermal breakthrough is greater for smaller surface area. This means an inverse relationship between L^2 and the arc cost. The elevation difference (h) between the producing and injecting zone is made linear to the arc cost due to the fact that injected fluid, being cooler and denser would tend to sink down the reservoir. Hence, it is intuitive that a deep

producing well would have a higher chance of communicating with an injection well, than a shallow, producing well would. Since h could be positive (producing zone below the injection zone) or negative, it appears in the equation as an exponential term e^{sh}, with a scaling factor s to keep it from dominating the rest of the weighting factors.

In a similar manner, producing and injecting rates during the tracer tests (q_{pt} and q_{rt}), can also be made as weighting factors. A well which produces at a small rate and manifests positive tracer return would have a higher likelihood of being affected by injection returns than another well which is producing at a higher rate with similar returns. Therefore, q_{pt}, and with the same logic, q_{rt}, are inversely related to the arc cost.

It is to be emphasized that all the factors need not be used to get the arc costs. Some factors could be deleted, and others weighed or included depending on which ones the developer deem to be important on the basis of reservoir behavior and information.

The sum of the arc costs from a particular injection well to all the producing wells is its cost coefficient. The unknown or decision variable is the reinjection rate, q_{ri}, into injection well i. The product of the injection rate and the arc cost is the breakthrough index for the specific arc or injection/production pair of wells as expressed by Equation (4).

$$b_{ij} = c_{ij} q_{ri} \tag{4}$$

The summation of breakthrough indices for all arcs is then the fieldwide breakthrough index B. Under the optimization strategy, it is this index which is the objective function that has to be minimized subject to well capacities and field operating constraints.

Two algorithms were used for optimization strategy:

1) linear programming which employs the simplex method, and
2) quadratic programming

Linear Programming

In the linear programming algorithm, the objective functions to be minimized are shown by Eqs. (5) and (6).

$$\text{Minimize } B_1 = \sum_{i=1}^{N_1} \sum_{j=1}^{N_2} c_{ij} q_{ri} \tag{5}$$

Subject to:

$$q_{ri} \le q_{ri\max}$$
$$\sum_i q_{ri} = Q_{rtot}$$
$$q_{ri} \ge 0$$

$$\text{Minimize} \quad B_2 = \sum_{i=1}^{N_1} \sum_{j=1}^{N_2} c_{ij} q_{pj} \tag{6}$$

Subject to:

$$q_{pj} \le q_{pj\max}$$
$$\sum_j q_{pj} = Q_{ptot}$$
$$q_{pj} \ge 0$$

where:
N_1 = number of injectors
N_2 = number of producers
q_{ri} = injection rate into well i
q_{pj} = producing rate from well j
q_{rimax} = maximum permissible rate into well i
q_{pjmax} =maximum permissible rate from well j
Q_{rtot} = total required injection rate
Q_{ptot} = total required producing rate

In this algorithm, the mutual dependence of injection and production rates is accounted for by alternately exchanging their roles as decision variables and weighting factors.

Quadratic Programming:

On the other hand, the formulation for the second algorithm is shown by Equation (7).

$$\text{Minimize} \quad B = \sum_{i=1}^{N_1} \sum_{j=1}^{N_2} c_{ij} q_{ri} q_{pj} \tag{7}$$

where the variables and constraints are the same and combined as in the first formulation. In this approach, the interdependence of injection and production rates is explicitly acknowledged by treating both as decision variables and including them in the objective function as a product.

Hence, the objective function becomes a quadratic and the problem is solved by a quadratic programming (QP) solver.

Preliminary Results Using Tracer Return Data

The results of the two radioactive tracer tests were used in the above algorithms. Specifically, the mean transit recovery time, the fraction recovered, the aerial and vertical separation between the injection and production pair of wells, the flowrates during the tracer tests, as well as the maximum flowrates of all the wells were used as input in the algorithms. In this test, it was assumed that only OK-12RD and PN-9RD are the reinjection wells. The problem calls for allocating the production rates among the different wells as the required total production rate decreases from 930 kg/s.

The results indicate that the two approaches or algorithms give similar results. As the required total field load decreased, the producing rates was reduced and production wells were shut in one-by-one depending on its potential damage to the field as manifested by the injector/producer cost coefficient. The higher the cost coefficient, the more serious is the potential for thermal breakthrough. However, the cost coefficients which enable the explicit ranking of the wells are present only in the linear programming algorithm. Nevertheless, the actual allocations provided by quadratic programming duplicate those of linear programming.

It can be concluded, therefore, that by knowing the arc costs, the programs obtain the optimal rate allocation for both injection and production wells.

3.5 USE OF CHLORIDE DATA

Due to economic and operational constraints, radioactive tracer cannot be injected into every reinjection well. Similarly, not all the production wells can be monitored during a tracer test. To find another parameter which can be used to optimize reinjection strategy, attention was turned to the reservoir chloride measurement of the production wells as shown later in Figure 20. It has been established by the PNOC geochemists that the chloride values of a producing well can be used as an indication of the extent of reinjection returns to this well. The correlation or strength of the relationship between the chloride of a producing well and the flowrate of an injecting well was obtained in four different ways. Figure19 shows in graphical form the different methods used to correlate the chloride values of a production well with the injection flowrates of an injection well. It should be remembered when comparing, that these numbers represent a relative assessment of the producer/injector pair potential for thermal breakthrough.

1. First, the correlation between the chloride value with time of a production well and the mass flowrate with time of an injection well was obtained (Figure 19a).
2. Second, the correlation between the chloride value with time of a production well and the total mass flowrate with time of an injection well was calculated (Figure 19b).
3. Third, the correlation between the deviation of the chloride value of a production well from the best fit line and the flowrate rate of an injection well was computed (Figure 19c).
4. Lastly, the chloride value with time of a production well was expressed as a linear combination of the mass flowrates of the injection wells.

The first method (Figure 19a) of chloride-flowrate correlation stems from the observation that the chloride values of a production well are affected when particular injection wells are disconnected from or hooked on line. If an injection well communicates strongly with a production well, then putting this injection well on line is usually followed by a substantial increase in the chloride measurements of the affected well. Once it is removed from service, there is an accompanying decrease in the chloride data of the producing well.

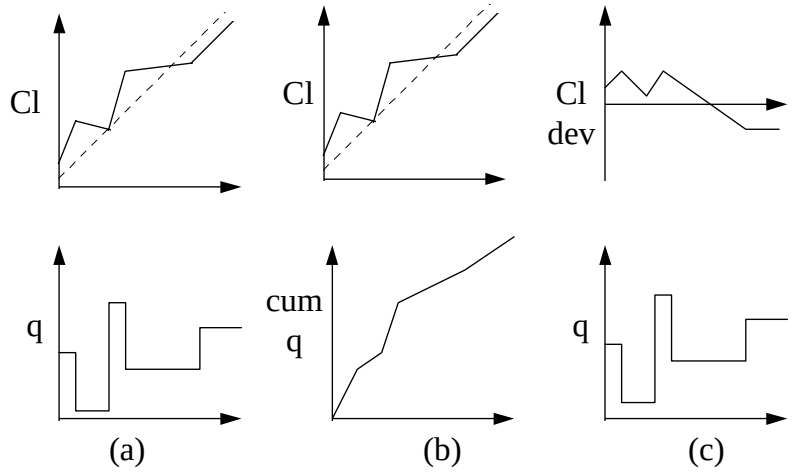

Figure 19: Chloride vs. Flowrate Correlation Methods

In the second method (Figure19b), what is examined is the relationship between chloride and the cumulative flow. Since the chloride value of a production well at a particular time is the cumulative effect, it is reasonable to see the relationship between this chloride value and the total flowrate of the injection well. Given the hypothetical case of an injection well affecting strongly a production well, the plots of the two variables with time would be similar to Figure 19b.

On the other hand, it is also desirable to examine the relationship between the magnitude of the increases in chloride value of a production well with the flowrate of an injection well. Going back to the hypothetical case, it would be logical to expect that the effect of a high injection rate would be a greater step change in the chloride value of the production well. The magnitude of this change

is measured by the deviation of the chloride value from the best fit line and this deviation is then correlated with the injection flowrate at that time (Figure 19c).

The effect of a particular injection well on a certain production well can be concluded unambiguously only when all other factors are held constant (such as injection flowrates of other injection wells and producing rates of all other wells are unchanged). This is complicated by the fact that a single injection well could interact with more than one production well. As a consequence, the net effect on a production well at a particular time interval would be due to the effects of the particular injection wells which were active in the same time interval. To take this into account, the last method seeks to express the chloride value of the production well as a linear combination of the injection flowrates of all the active reinjection wells at the concerned time. This is illustrated by Equation (8).

$$Cl_i = a_0 + \sum_{j=1}^{n} a_j q_j \qquad (8)$$

where:
Cl_i = chloride value of well i at time t
a_0 = initial chloride value at time t
a_j = correlation coefficient between production well i and injection well j
q_j = mass flowrate of injection well j
n = number of injection wells

The system of linear equations is put in matrix form and then solved simultaneously by a matrix solver like the Gauss-Jordan method of elimination.

Results of the Chloride Data Methods

The plots of the first three chloride methods are shown in Figures 20 to 27 using the wells OK-7, PN-9RD, PN-28 and PN-2RD. The first method is demonstrated by Figures 20 and 21, the second by Figures 22 and 23, and the third by Figures 24 and 25. Figures 26 and 27 have been included for comparison.

Figure 20a reflects the increase in monthly chloride values of well OK-7 and Figure 20b shows the monthly injection flowrates of PN-9RD. For an injector/producer pair with strong communication, it has been observed that the crests and troughs of the injection plot usually coincide with those of the producing well. This is reflected in high correlation coefficients during these times as demonstrated by Figure 21. In this case, this would infer and confirm that there is good communication between OK-7 and PN-9PD. The same effect was found to exist if the correlation is calculated with a shift in time of the chloride values of OK-7. This was done to accommodate

the reasoning that the increase in chloride value is an effect, and that there could be a lag or delay in the response of the producing well. In spite of the shift, the general trend of the correlation plot remained the same.

(a)

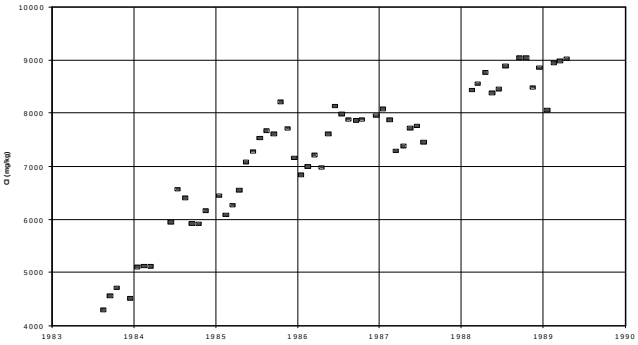

(b)

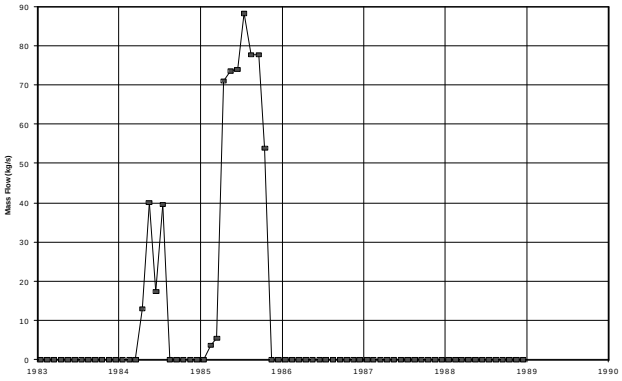

Figure 20: OK-7 Chloride and PN-9RD Flowrate

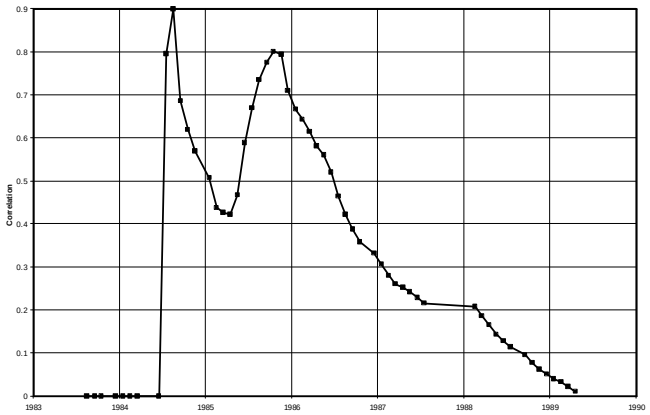

Figure 21: OK-7 / PN-9RD Chloride-Flow Correlation

Figure 22 shows the plot of the cumulative flowrate with time of PN-9RD. The correlation with time of the chloride data with total rate shown in Figure 23 remain remarkably high throughout. The same pattern has been demonstrated by the rest of the OK-7/injection well pairs. The other

plots of producing/injecting pairs show that the general trend for a particular production well remains the same with almost all the injection wells. This would indicate that this method cannot be used to assess and differentiate the relationship between a producer and an injector.

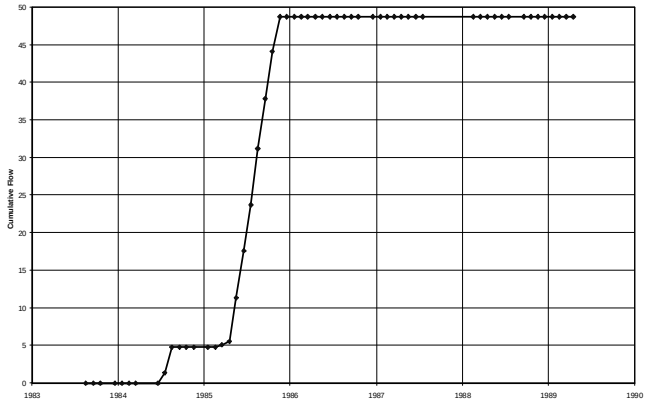

Figure 22: PN-9RD Cumulative Flow

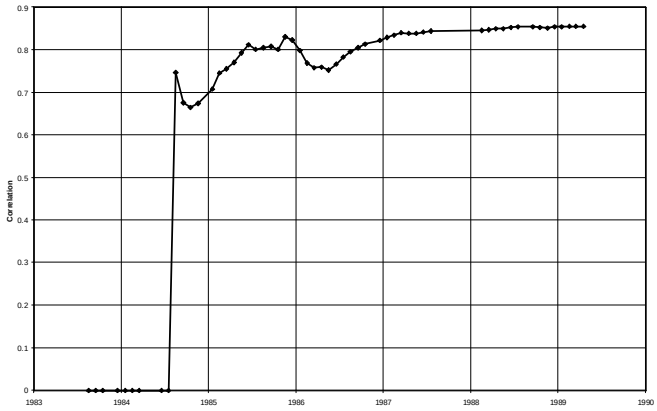

Figure 23: OK-7 / PN-9RD Chloride - Cumulative Flow Correlation

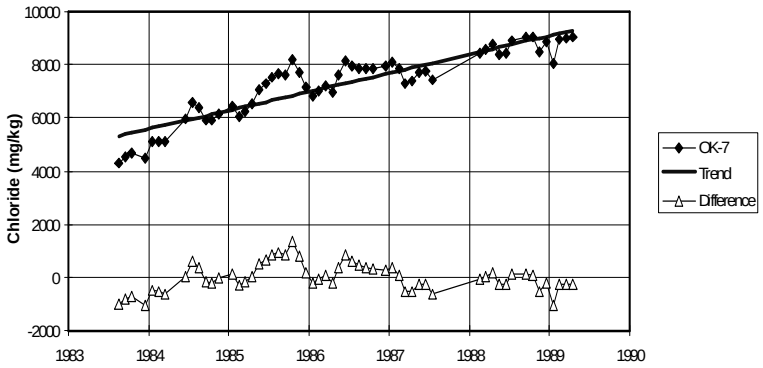

Figure 24: Trend and Deviation in OK-7 Chloride

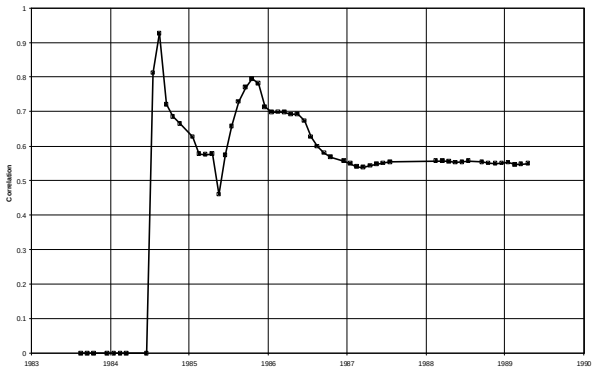

Figure 25: Correlation Between OK-7 Cl Deviation and PN-RD Flow

Figure 24 is the same plot of OK-7 monthly chloride, with the dashed line representing the linear regression fit to this curve. The deviations from this best fit line are plotted in Figure 24 and the correlation between the deviation and injection rate is shown in Figure 25. It can be seen that this plot of Figure 25 (Cldev-flowrate) and that of Figure 4 (Cl-flowrate) are similar.

(a)

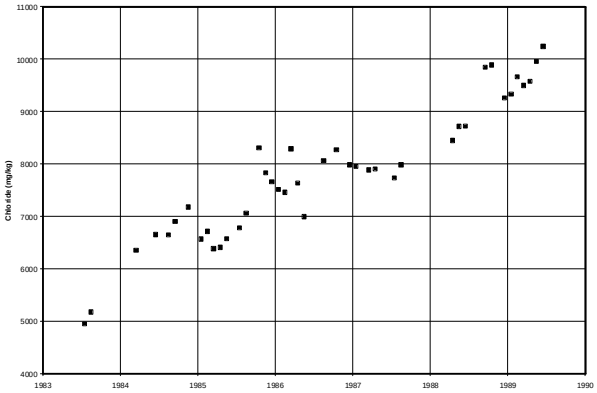

(b)

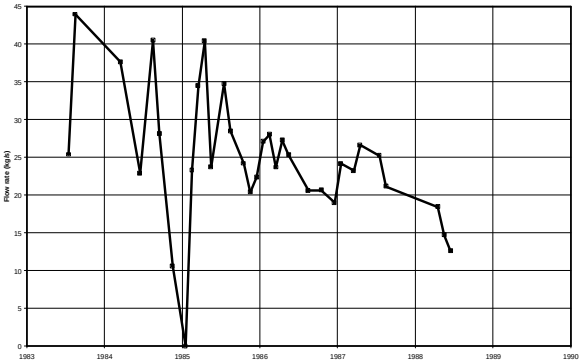

Figure 26: PN-28 Chloride and PN-2RD Flowrate

Figures 26a and 26b show the chloride values of PN-28 and the flowrates of PN-2RD. These are correlated and the results plotted in Figure27. One would note that the correlation values remain negative implying a lesser degree of interaction or communication between PN-28 and PN-2RD. When Figure 27 is compared with that of Figure 21, both being chloride-flowrate correlation, the immediate disparity in the relationship between OK-7/PN-9RD and PN-28/PN-2RD can be concluded,

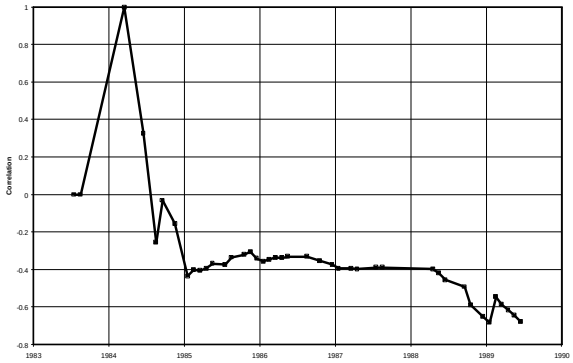

Figure 27: PN-28 / PN-2RD Chloride-Flow Correlation

Table 2:Summary of Chloride - Flowrate Correlations

		Reinjection Wells								
Production Wells	Method	PN-1RD	PN-2RD	PN-3RD	PN-4RD	PN-5RD	PN-6RD	PN-7RD	PN-8RD	PN-9RD
OK-10D	Cldev - Flow Corr	0.4320	-0.1310	-0.2740	-0.3800	-0.5690	0.3240	0.3590	-0.0330	-0.3910
	Cl - Flow Corr	0.3420	-0.2850	-0.0600	-0.3520	-0.4560	0.3320	0.4190	-0.0400	-0.3890
	Linear Comb Coeff	4.0440	-11.5100	1.7370	2.8710	-7.6590	4.1940	5.2960	2.6470	1.8320
OK-7	Cldev - Flow Corr	-0.1650	-0.1500	0.0270	0.4680	0.6140	-0.5050	0.9300	0.8160	0.9260
	Cl - Flow Corr	-0.4840	-0.4110	0.6370	0.4600	0.7790	-0.1310	0.9050	0.3730	0.9000
	Linear Comb Coeff	11.9300	-21.9200	28.5600	5.0000	11.2100	8.1530	-6.8300	20.9400	29.3800
PN-15D	Cldev - Flow Corr	0.2420	0.1510	-0.4700	-0.6670	-0.5340	0.3950	-0.4150	-0.5100	-0.7190
	Cl - Flow Corr	-0.2660	-0.5452	0.6250	0.5820	0.7840	0.3470	0.2620	0.5110	0.3040
	Linear Comb Coeff	12.9800	-19.0200	37.1400	-1.5330	-6.5890	5.3900	-0.2979	11.0600	0.2206
PN-26	Cldev - Flow Corr	0.0910	-0.1440	0.3050	0.3010	0.5460	-0.2830	0.7950	0.4000	0.5000
	Cl - Flow Corr	0.1150	-0.1260	0.7550	0.4520	0.5380	-0.3860	0.8010	0.1910	0.4730
	Linear Comb Coeff	9.4090	-14.7200	25.2200	5.4490	5.4890	7.6020	-6.2060	21.3000	17.0900
PN-28	Cldev - Flow Corr	0.4480	-0.1720	-0.0130	-0.0590	-0.0640	0.2230	0.5000	-0.2130	
	Cl - Flow Corr	-0.0190	-0.4050	0.6790	0.5600	0.5320	0.2670	0.7470	-0.2010	
	Linear Comb Coeff	9.7210	-8.9670	22.6100	-4.6030	15.1300	8.7520	-1.4170	-0.3865	
PN-30D	Cldev - Flow Corr	-0.0840	-0.2100	-0.1630	0.0040	-0.1020	0.1720		-0.2130	
	Cl - Flow Corr	-0.0900	-0.2470	-0.1620	-0.0640	-0.1020	0.1950		-0.2010	
	Linear Comb Coeff	1.0040	-7.3590	4.7760	7.5970	-5.4280	1.7240		-0.3865	

Table 2 gives a tentative summary of the coefficients obtained from the four chloride methods. The method of chloride-total rate correlation (the second method) has been disregarded and, therefore, not included in this tabulation. For the linear combination method, the table only shows the correlation taken for the whole data set. For the chloride-rate correlations, the numbers shown were either the average or those taken at the time the injection well has stopped injecting. The table shows:

1) In slightly more than half of the tabulated results, the calculated chloride-flowrate correlation is similar and very close to that of the chloride deviation-flowrate correlation. When only the signs of the correlation are compared, this increases to about 70%.
2) In general, the relationship shown by the linear combination coefficients agree with the observed relationships. For example, there is a high coefficient of correlation of OK-7 and PN-26 with PN-9RD, PN-8RD, and PN-1RD.

The limitation imposed by the two chloride-rate correlation methods (first and third) as shown by the dashed line is due to the fact that during the time considered the reinjection well was not injecting. Similarly, the linear combination method fails when the matrix is singular and no solution to the system of linear equations can be found.

3.6 SUMMARY AND CONCLUSIONS

The tracer return data, together with field geometry and operating conditions have been used to allocate production and injection rates among the Palinpinon wells using algorithms from Operations Research.

The theory behind the optimization strategy is that the reservoir can be visualized as a network of arcs connecting injector to producer. Each arc has a potential for thermal breakthrough caused by fluid flow from injector to producer and this potential is measured by the arc cost. The methods for optimization make use of linear programming and quadratic programming where the objective function to be minimized is the fieldwide breakthrough index defined to be the product of the arc cost and the flowrate.

The results of allocation are the same for both linear and quadratic programming. However, cost coefficients which provide a ranking of the injector/producer pair according to the potential for thermal breakthrough is provided only in linear programming.

Chloride was examined as another parameter for optimization since it has been observed to be an indicator of the extent of reinjection returns to a producing well. Four different methods of finding the correlation between the chloride value and the flowrate were examined. In general, there has been agreement between the chloride-rate correlation and the chloride deviation-rate correlation. The linear combination method also showed promise. The initial results of the study were encouraging and pointed out that the correlation between chloride and flowrate can be used as arc costs in optimizing production and reinjection strategy.

4. OPTIMIZATION OF WATER INJECTION INTO VAPOR-DOMINATED GEOTHERMAL RESERVOIRS

This study was conducted by Roman B. Sta. Maria and Roland N. Horne

4.1 SUMMARY

Water injection into a vapor-dominated geothermal reservoir is an effective method of sustaining steam production from the field. Injection puts additional water to the reservoir and raises the prevailing reservoir pressure. This process improves the field's productivity. However, the increased pressure also increases the water retention capacity of the reservoir rocks through the effects of adsorption and capillary condensation.

Due to the significant costs associated with water injection programs, optimizing injection not only involves maximizing the energy yield from the resource but also the present worth of the project. Two crucial parameters that need to be established are: 1) how much to inject; and, 2) when to inject it. This study investigated the optimal design of these parameters.

It was found that comparable energy yield can be attained for injection programs that are initiated at various stages of the field's development. Higher injection rates are desirable when the injection program starts later in the productive life of the field. Considering the economics of the project, it is best to implement the injection program during the later stages of the field's development. This way, a greater fraction of the injectate can become available for production and at the same time optimize the present worth of the project.

4.2 INTRODUCTION

The ability to model the effects of water injection into vapor-dominated reservoirs is of great interest to the geothermal industry. Experience has shown that vapor-dominated systems are prone to run out of water even though vast amounts of heat still remain in the reservoir. It has been established through research and field studies that water injection into the reservoir can provide artificial mass recharge to improve steam production from the field (Enedy et al, 1991). However, if done incorrectly, injection may have detrimental effects on production (Barker et al., 1991). Clearly, an appropriate injection program is a major component of resource management strategy for vapor-dominated geothermal reservoirs.

Adsorption and capillary pressure are major factors affecting the behavior of vapor-dominated geothermal reservoirs. These mechanisms affect both the estimation of the reserves and the production performance of the field. The effectiveness of water injection programs to sustain the field's productivity is also affected. Hence the optimization of an injection strategy should include consideration of these effects.

Physical adsorption is the phenomenon by which molecules of steam adhere to the surfaces of a porous medium. This phenomenon is caused mainly by Van der Waals forces. When sufficient deposition has taken place, a capillary interface may form and deposition due to capillary condensation becomes more significant (Horne et al., 1995). In addition, the surface between the vapor and the liquid phases in a porous medium is not flat. It is a well-recognized phenomenon that the vapor pressure above the curved surface of a liquid is a function of the curvature of the liquid-vapor interface. Thus, curved interface thermodynamics is more appropriate than flat interface thermodynamics. The curvature of the surface gives rise to vapor pressure lowering (VPL), thus allowing liquid and vapor to coexist in equilibrium at pressures that are less than the saturation pressure.

Understanding how adsorption and capillary forces affect water injection is particularly relevant at this time because of the plans to increase water injection into The Geysers geothermal field. Although water injection has been ongoing for many years, injection rates will increase significantly when water from Lake County, and possibly the city of Santa Rosa, becomes available for injection.

Numerical simulation is an effective method to forecast the performance of a geothermal reservoir. Until recently, simulators have used flat interface thermodynamics to define the phase of the reservoir. However, the development of new simulation codes has enabled the effects of adsorption and curved interface thermodynamics to be incorporated. This study made use of these simulators to investigate of the effects of adsorption and capillary pressure on water injection into geothermal reservoirs. The ultimate objective is to optimize water injection into a hypothetical vapor-dominated geothermal field.

4.3 PRELIMINARY WORK

The simulator TETRAD was used in this study. TETRAD is a commercial simulator that has been modified to account for vapor pressure lowering (VPL). Version 12 of this simulation code uses the generalized vapor pressure lowering algorithm developed in the Idaho National Engineering Laboratory (Shook, 1993). This algorithm follows-up on an earlier work by Holt and Pingol (1992) to modify the standard steam tables to account for vapor pressure lowering.

The data required to incorporate vapor pressure lowering in numerical simulations is either a capillary pressure relationship (p_c versus S_w) or an adsorption isotherm. TETRAD requires a p_c versus S_w relationship like the one shown in Figure 28.

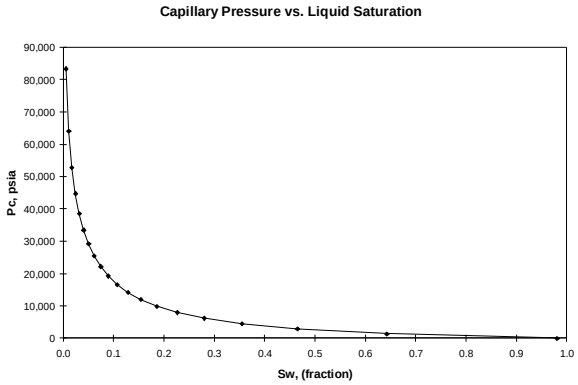

Figure 28: Capillary pressure relationship.

This capillary pressure relationship was based on the adsorption isotherm shown in Figure 29. The two sets of data are equivalent and conversion from one to the other is done through the Kelvin equation and an intermediate relation for X vs. S_w. For more details, refer to the paper by Sta. Maria and Pingol (1996).

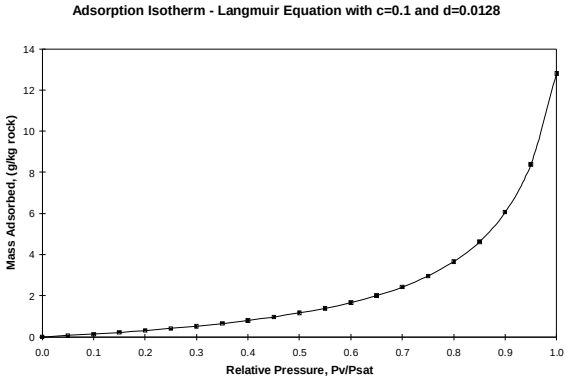

Figure 29: Typical Geysers adsorption isotherm.

4.4 THE RESERVOIR MODELS

Two vapor-dominated reservoir models (with simple geometry) were developed to investigate the effects of adsorption and capillarity on injection. The geometry of these models are illustrated in Figure 30 and Figure 31. The basic properties used in both models are listed in Table 3. The relative permeability function used causes steam to be the only mobile phase at the given initial water saturation. Water becomes mobile when S_w is greater than 35%. Adsorption properties are patterned after those typically observed in The Geysers.

The model shown in Figure30 is comprised of a horizontal layer 1,000 feet long, 200 feet wide, and 100 feet thick. A uniform Cartesian grid with a total of five gridblocks was used. The porosity, permeability, sorption properties, and capillarity are uniform for all gridblocks. Initial thermodynamic state (pressure, temperature, and saturation) is also uniform. An injection well and a production well were located on the opposite ends.

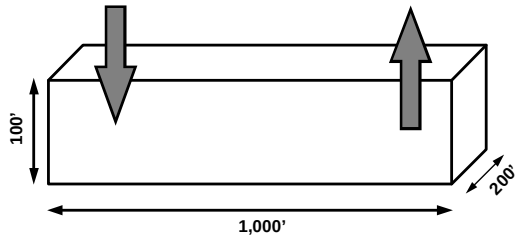

Figure 30: One-dimensional model (Cartesian grid) with a pair of injection and production wells.

The second model shown in Figure31 uses a uniform radial grid. The model is horizontal, 100 feet thick, and 1,000 feet in diameter. This model uses the same properties used in the Cartesian model. However, in this case the production and injection wells are both located on the center gridblock.

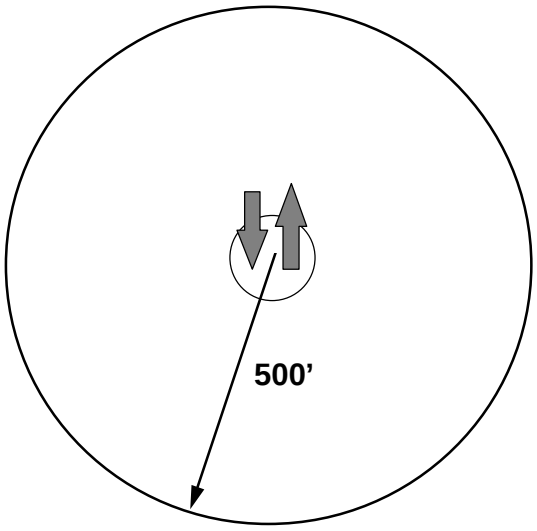

Figure 31: Horizontal two-dimensional model (radial grid) with a pair of production and injection wells located at the center.

The two models are essentially closed tanks. The model boundaries are closed to mass and heat flows. The only way mass and energy can flow in and out of the systems are though the wells.

Table 3: Properties of the Cartesian and radial model.

Porosity	5%
Permeability	20 md
Initial liquid saturation	30%
Initial reservoir pressure	400 psia
Reservoir temperature	Evaluated

For clarity, the "reservoir pressure" of 400 psia shown in Table3 is equal to the pressure of the vapor phase. Note that the reservoir temperature needs to be evaluated based on the given reservoir pressure and the prevailing phase saturation in the reservoir. At the given initial condition wherein S_w is 30%, the appropriate reservoir temperature is about 465°F. If we are using flat interface thermodynamics, the appropriate temperature would have been 445°F. In a conventional sense the models we are using are superheated by about 20°F at the initial condition.

4.5 EFFECTS OF INJECTION

Working with the one-dimensional Cartesian model, we investigated the effects of water injection into a vapor-dominated reservoir when adsorption and vapor pressure lowering are considered. We compared the predicted behavior to the case when adsorption and vapor pressure lowering are ignored.

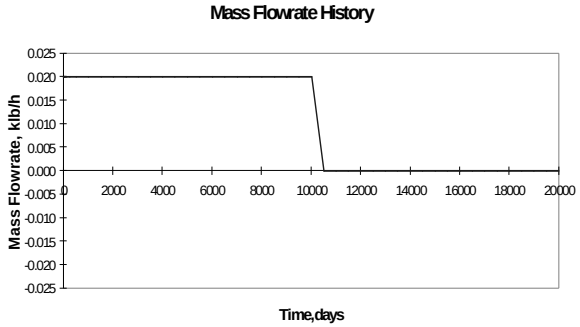

Figure 32: Constant water injection for 10,000 days for the one-dimensional Cartesian model.

The reservoir was perturbed by injecting cold water (90°F). Figure 32 shows that 20 lbs/h of water is injected during the first 10,000 days. Afterwards, the field was shut-in and the reservoir allowed to equilibrate.

Figures 33, 34, and 35 contrast the behavior of the reservoir if it is modeled with and without adsorption and vapor pressure lowering. Shown in these plots are the reservoir pressure, reservoir temperature, and phase saturation measured in the injection gridblock.

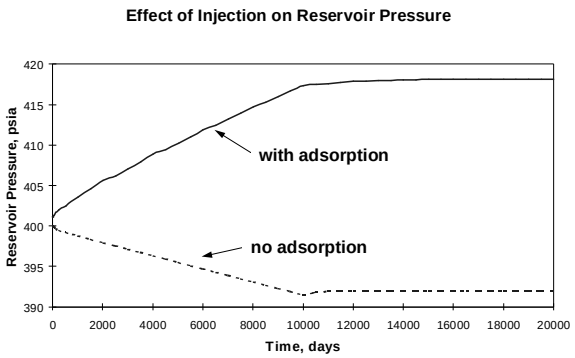

Figure 33: Pressure behaviors of the injection gridblock.

Figure 33 shows the reservoir pressure through time. With no adsorption the pressure measured in the injection gridblock is observed to decline. With adsorption the opposite effect is observed. Instead of declining, the pressure is observed to rise in response to injection.

Figure 34 shows the reservoir temperature through time. As mentioned earlier, the use of pressure as the independent parameter to specify the thermodynamic state of the reservoir result in different temperatures for models with and without vapor pressure lowering. Without adsorption, the reservoir temperature is about 445 ^{o}F; this is the saturation temperature at 400 psia if the vapor/liquid interface is flat. With vapor pressure lowering, 400 psia actually corresponds to a lowered vapor pressure across a curved vapor/liquid interface. With the water saturation initially at 30%, the given adsorption isotherm dictates the appropriate reservoir temperature to be about 465 ^{o}F. Thus, in terms of initial energy in-place the models with and without adsorption are not equivalent. The differences are not limited to the heat in-place but also on the temperature variation of each gridblocks. Without adsorption, temperature declines monotonically for all gridblocks. With adsorption, the gridblocks adjacent to the injection gridblock initially exhibit increasing temperature before starting to decline (not shown in Figure 34).

A curious behavior of the reservoir pressure is illustrated below. Shown in Figure 35 are the reservoir pressures measured in the injection and production gridblocks through time. The pressure in the injection gridblock was initially higher than the production gridblock. However, after 4,000 days the situation is reversed; the production gridblock have higher pressure than the injection gridblock. However, throughout the entire injection period there is a net mass flowing away from the injection gridblock towards the production gridblock.

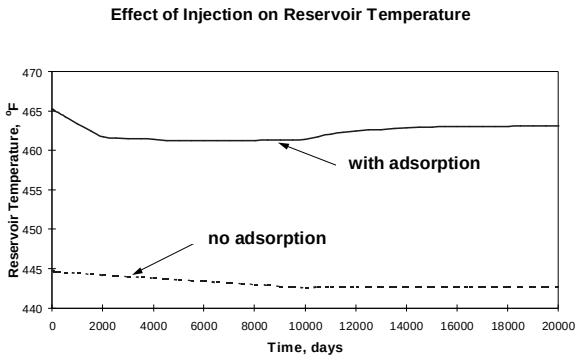

Figure 34: Temperature behaviors of the injection gridblock.

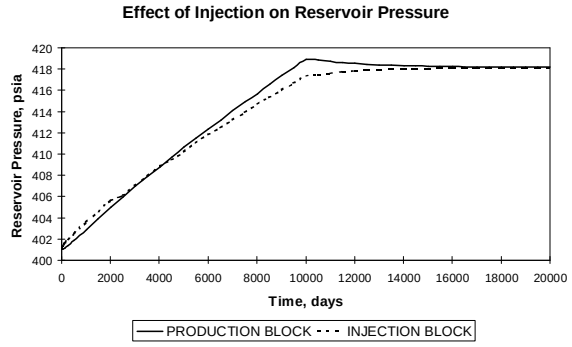

Figure 35: Pressure responses of the injection and production gridblocks.

The apparent contradiction in pressure gradient and mass flow is explained by keeping in mind that the pressure of the vapor and liquid phases are different. As defined earlier, the reservoir pressure shown in Figure 35 is the pressure of the vapor phase. Thus, initially steam is migrating away from the injection gridblock. At a later time, the pressure gradient is reversed and steam migrates towards the injection gridblock. On the other hand, water will continuously move away from the injection gridblock towards the production gridblock.

The pressure of the water phase is always higher in the injection gridblock than the production gridblock, or any other adjacent gridblocks. This can be explained if we consider the saturation variation between gridblocks as shown in Figure 36. The vapor saturation of the injection gridblock is less than the production gridblock. From Figure 28 we know that the capillary pressure increases as the vapor saturation increases (i.e., decreasing liquid water saturation). Capillary imbibition draws water from the injection area towards the production area. Even though there is a counter-flow of steam and water, the net mass flow is still directed away from the injection area.

To complete the picture, Figure37 shows the reservoir temperature measured in the injection and production gridblocks.

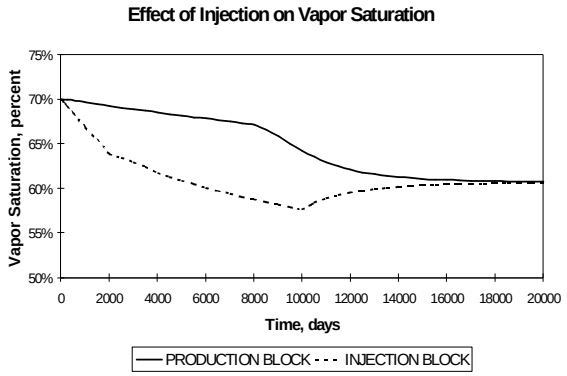

Figure 36: Vapor saturation changes measured in the injection and production gridblocks.

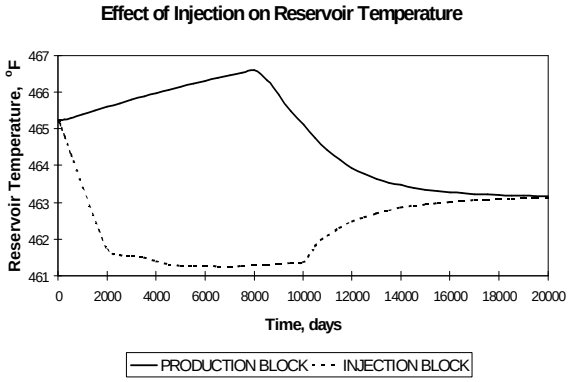

Figure 37: Temperature responses of the injection and production gridblocks.

The next step was to use the two-dimensional radial model to investigate the behavior of the reservoir when we try to produce the injected water. To do this, we imposed adsorption and vapor pressure lowering on the model. During water injection, the reservoir pressure is raised above the initial reservoir pressure. After terminating injection, the production well was opened. Production is constrained such that the maximum production rate does not exceed the injection rate and the well is able to produce only down to the point when the reservoir pressure is restored to its initial value.

Figure 38 shows the reservoir pressure throughout the 30,000 days simulation period. There was constant rate injection from 5,000 to 10,000 days. The production well is opened beginning at 15,000 days. The well is allowed to produce as long as it can sustain production based on the given constraints.

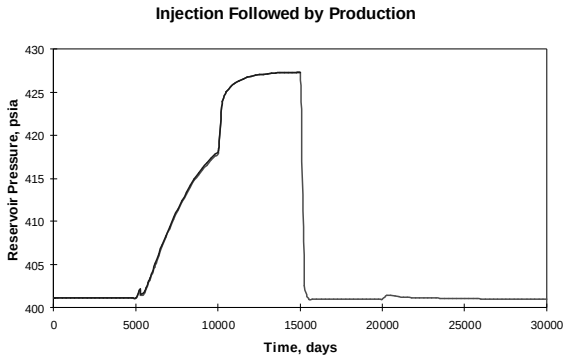

Figure 38: Pressure behavior of the central block in response to injection followed by production.

Figure 39 shows the resulting mass flowrate history of the model. We used a sign convention such that injection is denoted by a positive mass flow while production is denoted by negative mass flow. It is apparent from the plot below that the production rate declines rapidly in response to the decline of the reservoir pressure.

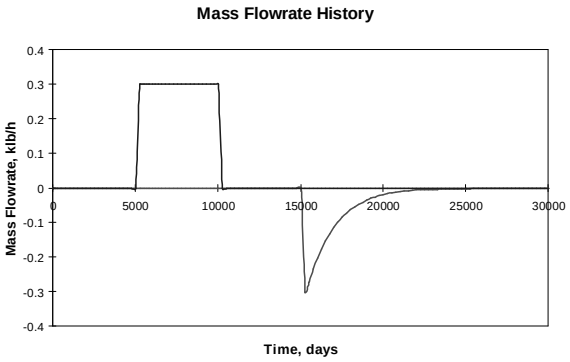

Figure 39: Injection and production rate history.

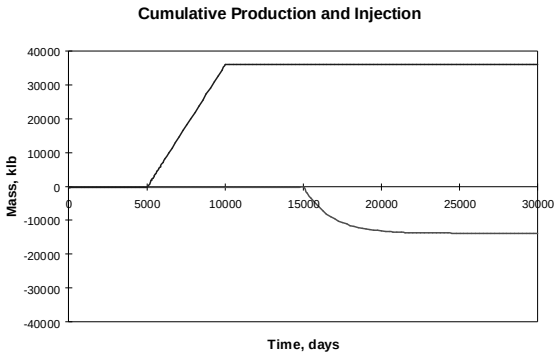

Figure 40: Cumulative masses produced and injected.

Figure 40 shows the same information as the previous plot but in terms of cumulative production and injection through time. The total mass injected into the reservoir is 36×10^6 lbs. The total mass produced afterwards is about 13.82×10^6 lbs. The total mass produced amounts to only 38.4% of the mass injected. The mass difference of over 22×10^6 lbs is retained in the reservoir and will be produced only if the reservoir pressure is allowed to decline below 400 psia.

4.6 OPTIMIZATION OF INJECTION

A field-scale model of a geothermal reservoir is necessary to study the optimization of water injection projects. The objective of this study is to determine the appropriate injection strategy that would result to an optimum energy yield from the geothermal resource while maximizing the net present worth of the injection project. There are two main questions what will be addressed in this study. How much water to inject and when to start injecting?

The Reservoir Model

A field-scale model of a hypothetical vapor-dominated geothermal reservoir was developed. The lateral extent of the reservoir is arbitrarily defined to be 7,000 feet by 7,000 feet. The vertical extent of the reservoir is 7,200 feet. The top of the reservoir is located at 2,000 feet below the ground surface. The basic properties of the reservoir model are listed on Table 4.

Table 4: Reservoir properties of the full-field model.

PROPERTIES	VALUES
Porosity	5%
Lateral permeability	40.008 md
Vertical permeability	20.004 md
Initial liquid saturation	35%
Initial reservoir pressure	400 psia

Reservoir temperature	Evaluated

Single porosity formulation was used to construct the reservoir model. Comparison of models constructed using single and dual porosity formulations shows that there is no significant difference in model performance during production. For the dual porosity model, it was assumed that the fractures also have adsorption properties identical to the matrix. This was a necessary assumption to have an initial mass in-place in the dual porosity model that was equal to that of the single porosity model. Another reason is to enable the use of curved interface thermodynamics in both the matrix and fracture gridblocks. However, the issue of how fractures should be treated with respect to adsorption property is still unknown question. Therefore, single porosity formulation was used to simplify the model and avoid the complications associated with the dual porosity formulation..

The lateral permeability value of 40.008 md given in Table4 is equivalent to that of a fractured system with a matrix permeability of 0.01 md (4% bulk porosity) and a fracture permeability of 200 md (1% bulk porosity). The vertical permeability was arbitrarily defined as 50% of the lateral permeability.

The relative permeability functions used were based of the work of Sorey (1980). The liquid and vapor permeability functions are defined as follows:

$k_{rl} = S_w^{*4}$; and,

$k_{rv} = (1-S_w^{*2})(1-S_w^{*})^2$

where $S_w^{*} = (S_w-S_{wc})/(1-S_{wc})$ and $S_{wc} = 0.35$.

Because the initial liquid saturation of the reservoir was set to 35%, only the steam phase is mobile initially. The liquid phase can become available for production by evaporation or if it becomes mobile when the liquid saturation rise above 35% through steam condensation or influx of additional water through injection.

Similar to the previous evaluation models, the field-scale model is essentially a closed tank. The model boundaries are closed to heat and mass flows. The only way heat and mass can flow to and from the reservoirs is through the production and injection wells.

The Field Model

The installed generating capacity of the field is 75 MW(e). Assuming a plant capacity factor of 90%, the average gross generating capacity of the field is 67.5 MW(e). The steam usage is 18.5 klb/h per MW(e). Thus, the required average production rate from the field to sustain full

generating capacity is about 1,250 klb/h. It was assumed that a minimum flowing bottomhole pressure of 100 psia is required to deliver steam to the power plant.

The field is located at an elevation of 2,000 feet above the source of water for injection. All injection water will be coming from this source. A 10-mile water pipeline brings water from the lowland source to the geothermal field.

Injection Optimization Scheme

Instead of modeling the entire reservoir, a symmetry element 1/50 the size of the reservoir is modeled. This symmetry element have dimensions of 1,400 feet by 1,400 feet laterally and 3,600 feet thick. If the full-scale reservoir is gridded into 5×5×2 layers, one gridblock will be represented by the symmetry element.

The symmetry element was further gridded into 7×7×9 layers. Each gridblock have dimensions of 200-by-200 feet and 400 feet thick. A pair of production and injection well are placed on diagonally opposite corners of the element. The injection well was completed in layer 5. The production well was completed in layers 4, 5, and 6. An observation well is placed in the center of the element and completed in layer 5. This production and injection wells placements implies that the field was developed with a five-spot pattern.. All subsequent measurements of the reservoir properties were conducted in layer 5.

Assuming that mass is produced uniformly throughout the reservoir, the field's total average production rate of 1,250 klb/h translates to a production rate of 25 klb/h for each symmetry element. For all subsequent simulation runs, the production rate of 25 klb/h will be referred to as the peak production rate. The water injection rates will be scaled relative to this peak production rate.

To investigate the issue of when should injection begin during the field's development, seven cases were considered. For all of these cases, production begins at time t=0 years while the injection operation begins at various stages of the field's exploitation. The cases considered are the following:

Case I: Injection begins at t = 0 year;
Case II: Injection begins at t = 5 years;
Case III: Injection begins at t = 10 years;
Case IV: Injection begins at t = 15 years;
Case V: Injection begins at t = 20 years;
Case VI: Injection begins at t = 25 years; and,

Case VII: Injection begins at t = 30 years.

For each of the cases above, the effects of injecting water at different rates were further investigated. These sub-cases are the following:

Case A: Base case - no injection;
Case B: Inject 20% of the peak production rate;
Case C: Inject 40% of the peak production rate;
Case D: Inject 60% of the peak production rate;
Case E: Inject 80% of the peak production rate;
Case F: Inject 100% of the peak production rate;
Case G: Inject 120% of the peak production rate;
Case H: Optimum case - injection rate causing water breakthrough at t = 50 years.

The cases described above required a total of 50 permutations. The optimum case (Case H) uses water breakthrough in the production well at t = 50 years (18,250 days) as the optimization criteria. The optimum injection rate may be less than or greater than the rate used in Case G (120% of peak rate).

Results

The first simulation performed was intended to establish the base case production performance of the reservoir. The production well was opened at t = 0 days and allowed to flow for 50,000 days. The production rate was constrained to a maximum rate of 25 klbs/h. The production well's bottomhole flowing pressure was constrained to a minimum of 100 psia. The base case production performance (first 20,000 days) is illustrated in Figures41, and 42.

Figure 41 shows that the reservoir can sustain peak production rate for about 7,000 days, or 19 years. After 19 years, the steam production rate declines exponentially with a nominal rate of about 0.12 per year.

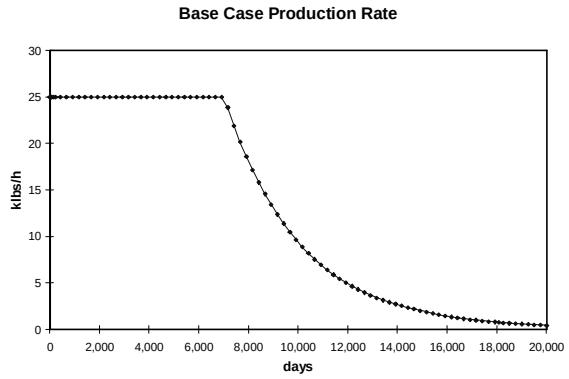

Figure 41: Base case production rate.

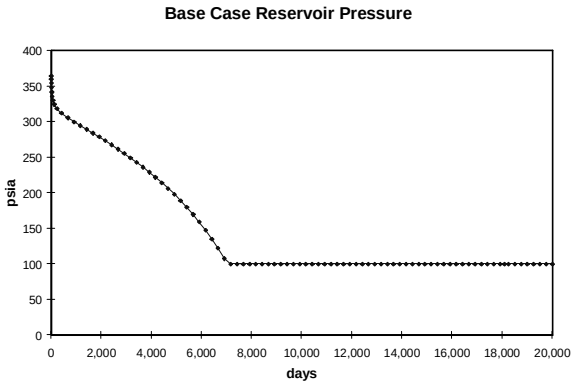

Figure 42: Base case reservoir pressure in the production gridblock.

Figure 42 shows the reservoir pressure measured in the production gridblock through time. After a rapid drawdown, the reservoir pressure declined gradually as steam from the neighboring areas migrate into the production area. The bottomhole pressure constraint of 100 psia was reached after 19 years of production.

To illustrate the production optimization process, shown in the following plots are results for Case I. In this case, injection and production begins at the same time at t = 0 years.

Figure 43 and Figure 44 are plots of the reservoir pressures through time measured in the production and observation gridblocks, respectively. In this case, the optimum injection rate is 93% of the peak production rate. It is clear from these plots that higher injection rates provide greater support to the reservoir pressure.

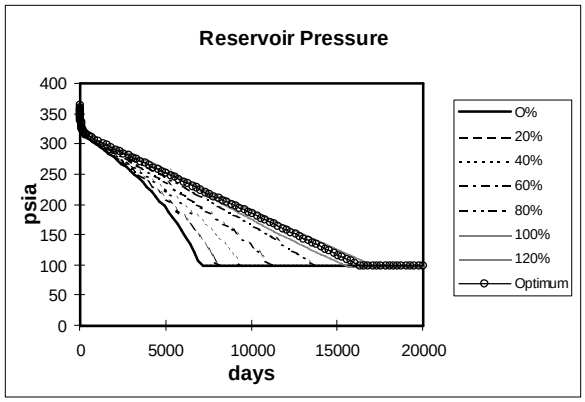

Figure 43: Case I - Reservoir pressures measured at the production gridblock.

Pressure support from injection translates to increased deliverability. Figure 45 shows that the steam production rate of 25 klb/h can be sustained much longer than the base case. Thus, the cumulative production is also increased. This is shown in Figure 46.

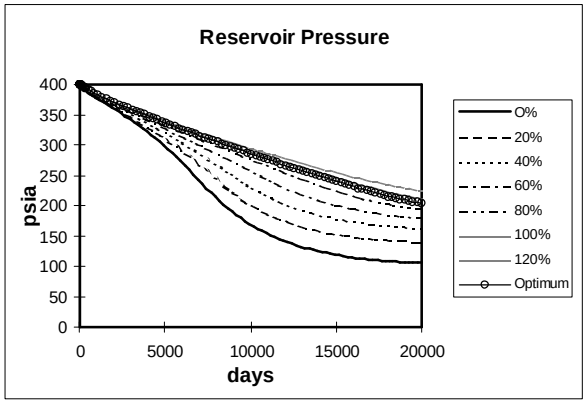

Figure 44: Case I - Reservoir pressures measured at the observation gridblock.

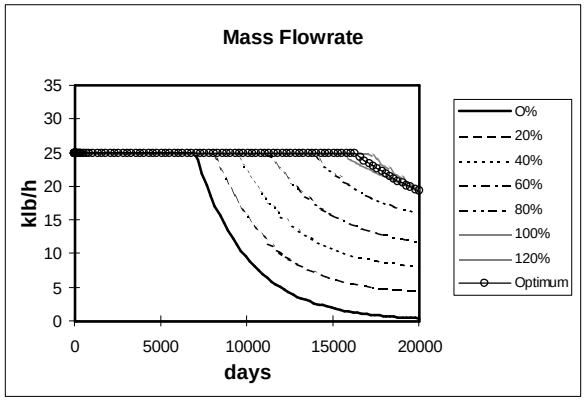

Figure 45: Case I - Steam production rates.

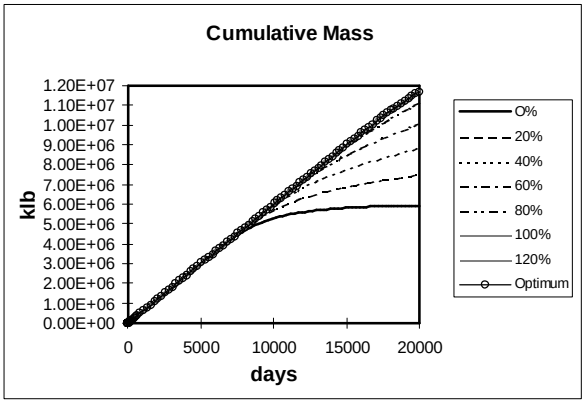

Figure 46: Case I - Cumulative masses produced.

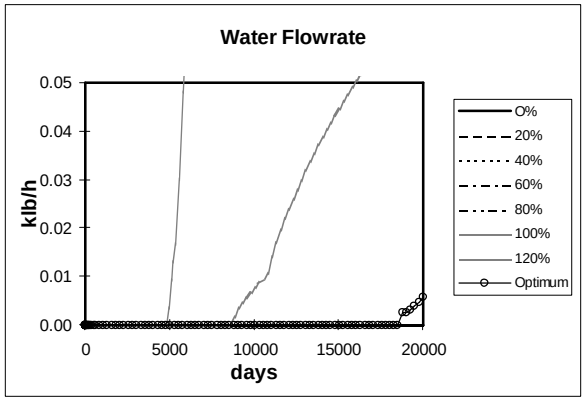

Figure 47: Case I - Water production rates.

As mentioned earlier, the criteria used to determine the optimum injection rate is the onset of water breakthrough in the production well at the 50th year. Figure 47 shows the water production rates for various injection rates of Case I. Injecting 100% and 120% of the peak production rate caused early breakthroughs. Injecting 93% of the peak rate satisfied the optimum criteria. Injecting water with a higher rate will cause water to breakthrough before the 50th year.

The optimum injection rates for all seven cases are shown graphically in Figure 48. There is a clear trend that starting water injection later in the field's development results to higher allowable injection rates. For example, Case VII where injection started in the 30th year of production, the optimum injection rate is 224% of the peak production rate.

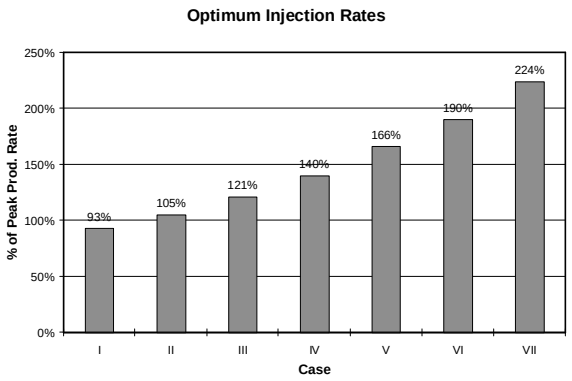

Figure 48: Optimum injection rates relative to the peak production rate.

The resulting optimum incremental production for each of the cases are shown in Figure 49. Except for Case VI and Case VII, the optimum incremental production is in excess of 80% of the base case. The lower incremental production of Cases VI and VII are mainly due to the limited production period after the start of injection.

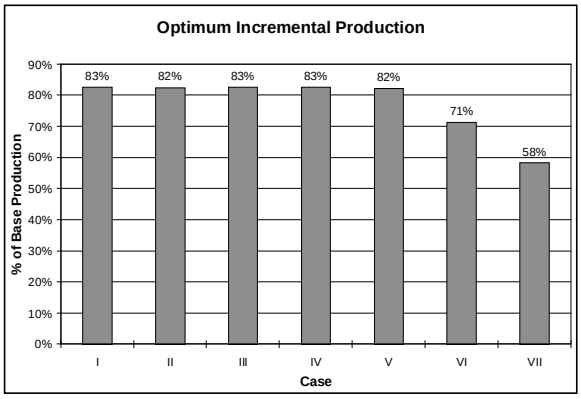

Figure 49: Optimum incremental production relative to the base production.

Another interesting parameter is how much of the injected water is eventually produced. Injectate recovery is defined as incremental mass produced (with injection) divided by the base case production. The injectate recoveries for all the cases are shown in Figure 50. It is clear from this graph that injection recoveries are lower for higher injection rates. In Case IV, injecting 20% (Sub-case B) results to a recovery of about 57%. Injecting 120% (Sub-case G) have a recovery of 48%. For the optimum case (Sub-case H), injecting 140% results to a recovery of only about 46%.

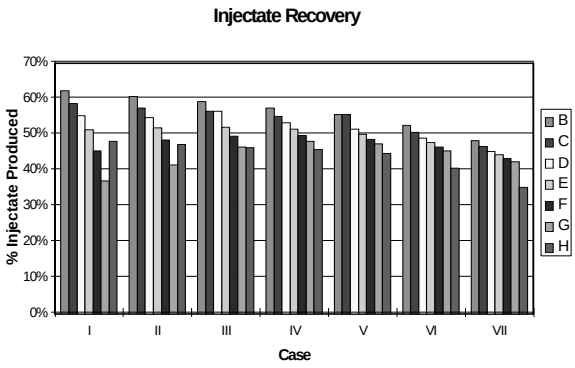

Figure 50: Injectate recovery for all cases.

Economic Optimum

Several assumptions were made about the field model and these were used to construct an economic model. We used this economic model to determine which of the cases previously considered yields the maximum present worth. Only the incremental costs and benefits of the injection project were considered because the costs and benefits associated with the base case are common to all the cases.

Incremental steam production is converted to incremental generation using the steam rate of 18.5 klb per MWh (net). The gross income from this incremental generation is evaluated using an assumed income of $25 per MWh. Using the cash flow method, a discount rate of 10% per year was used to account for the time value of money.

As mentioned earlier, the field is located at an elevation of 2,000 feet above the water source. All injection water will come from this source through a 10-mile water pipeline. These information were used to evaluate the capital expense required to build the pipeline and the pumping facilities. Building the pipeline costs $12 per diameter inch-feet installed. The pump's capital cost is $1,341/kW ($1,000/hp). The needed structures, controls, and power supply for the pump costs $2,682/kW ($2,000/hp).

For the full-field injection rates ranging from 250 klb/h (20%) to 3,000 klb/h (240% of peak rate), the combination of pump and pipeline sizes were optimized with the objective of minimizing the required capital expense for a given injection rate. With a choice of using either a 6, 12, 18, 24, or 30 inches diameter pipe, the power needed to pump water to the required elevation and also account for frictional pressure drop in the pipeline was evaluated and optimized. The optimum cases are given in Table 5. The total capital cost shown (pumping facilities and pipeline) is scaled to the size of the symmetry element (1/50 of the whole field).

Table 5: Optimum pump and pipeline facilities.

% Injection	Pipe Size (Inches)	Pump Power (kW)	Capital Cost (k$)
20%	6	285	99
40%	6	1,132	167
60%	12	645	204
80%	12	942	228
100%	12	1,308	257
120%	12	1,762	294
140%	12	2,318	339
160%	18	1,704	365
180%	18	1,975	387
200%	18	2,267	411
220%	18	2,582	436
240%	18	2,922	463

There are two other information required to complete the economic model. These are the operating cost of the injection system and the cost of the water injection wells. The cost of the pipelines to distribute water among the injection wells was ignored.

The operating the cost was estimated as a function of the total mass of injected water. By making assumptions on the cost of electricity to operate the pumps, the operating cost function of $0.11 per klb of water was used.

It was also assumed that a total of six injection wells is required to develop the field. If the average cost of drilling a well is $1.5 million, the total cost for the injection wells is $9 million. Scaling to the symmetry element (1/50), the cost of the injection well attributed to the symmetry element is $180,000.

A cash flow was generated for each of the cases considered previously. The net present worth of the injection project was evaluated using the assumed discount rate. Figure 51 below shows the graph of the present worth of all the cases.

For all cases, the optimum injection rates (Case H) gives the maximum present worth for that particular case. Comparing all the cases, the optimum present worth is $966,000 for Case IV. This is followed closely by Case V with $956,000. For Case IV and Case V, the injection started at the 15th and 20th year, respectively. Most likely, the real optimum occurs when injection starts between 15 and 20 years of the field's operation. Injecting earlier than the 15th year requires capital expenditure that are sooner than necessary. Injecting later than the 20th year requires higher injection rates; thus, higher capital expenditures. Furthermore, there will be loss of

opportunity to produce at peak rate because production from the field starts to decline after 19 years.

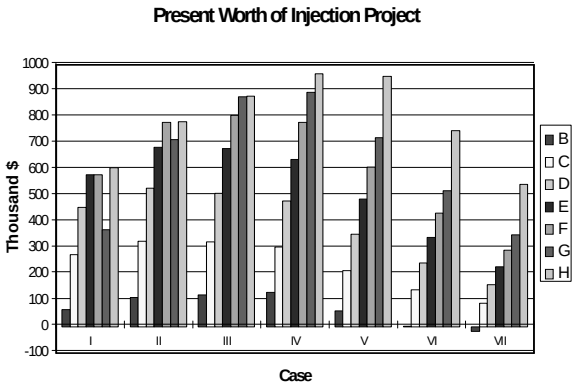

Figure 51: Present worth of injection project for all cases.

The cases discussed in this paper are all hypothetical. Therefore, the models and forecasts are not directly applicable to real fields. However, the same optimization process can be applied to a real field to assist in the development of an appropriate injection program.

4.7 CONCLUSIONS

This study shows that adsorption and capillary pressure are major factors governing the behavior of vapor-dominated geothermal reservoirs. These mechanisms affect both the resource size estimation and the production performance of the field.

The effectiveness of water injection programs to sustain the geothermal field's productivity is affected by adsorption and capillary pressure. Water injection into vapor-dominated reservoirs provides pressure support and mass recharge to the reservoir. Although this improves productivity, it also increases water retention in the reservoir through adsorption and capillary condensation.

Comparable mass and energy yield can be attained for injection programs starting at various stages of the field's exploitation. Higher injection rates are desirable when injection starts later in the life of the project. From the perspective of economics, an injection program intended to sustain the productivity of the reservoir is best implemented during the later stages of the field's productive life. This way, a greater fraction of the water injected becomes available for production yet optimizing the benefits of the time value of money.

5. STEAM-WATER RELATIVE PERMEABILITY

This work was conducted by Willis Ambusso, Cengiz Satik and Roland N. Horne, with the assistance of Nia Fong and Thembile Mtwa.

5.1 SUMMARY

A set of relative permeability relations for simultaneous flow of steam and water in porous media have been measured in steady state experiments conducted under the conditions that eliminate most errors associated with saturation and pressure measurements. These relations show that the relative permeabilities for steam-water flow in porous media vary approximately linearly with saturation. This departure from the nitrogen/water behavior indicates that there are fundamental differences between steam/water and nitrogen/water flows. The saturations in these experiments were measured by using a high resolution X-ray computer tomography (CT) scanner. In addition the pressure gradients were obtained from the measurements of liquid phase pressure over the portions with flat saturation profiles. These two aspects constitute a major improvement in the experimental method compared to those used in the past. Comparison of the saturation profiles measured by the X-ray CT scanner during the experiments shows a good agreement with those predicted by numerical simulations. To obtain results that are applicable to general flow of steam and water in porous media similar experiments will be conducted at higher temperature and with porous rocks of different wetting characteristics and porosity distribution.

5.2 INTRODUCTION

The concept of relative permeability is an attempt to extend Darcy's law for single-phase flow of a fluid through porous media to account for simultaneous flow of several phases. In this regime the flow of each phase is governed by the microscopic pressure gradient of each phase and the fraction of the overall permeability that is associated with it. This fraction, normally expressed as a fraction of the medium's permeability to single-phase fluid normally the wetting phase, is called the relative permeability. Since being introduced by Buckingham in 1907 and used extensively by investigators in the 1930's, relative permeability has been traditionally expressed as a function of saturation principally because it was believed that it depended on the pore volume occupied by the fluids (Hassler, 1944). Whereas a great many experiments have shown this to be true, a number of other experiments have shown that relative permeability depends on several other parameters such as interfacial tension, wetting characteristics and viscosity ratios of the flowing fluids (Fulcher et al., 1983; Osoba et al., 1951). Since these parameters are expected to change with the type of fluid, porous media and even with temperature, it should be expected that relative permeability would change for a given set of materials and experimental conditions. In addition it is necessary to define

residual saturations which normally indicate the smallest saturation for a given phase to become mobile. The curves and the residual saturations together define the relative permeability relations. For most cases these relations can be expressed as simple mathematical functions (Corey, 1954; Brooks and Corey, 1964).

Application of Darcy's law to the description of simultaneous flow of two or more phases of fluids in a porous medium requires the use of relative permeability relations (Hassler, 1944; Osoba et al., 1951; Corey, 1954; Brooks and Corey, 1964). In most applications in petroleum engineering such as those involving the flow of oil and water as in water flooding and oil and gas as in gas injection, these relations are well known and can be determined from routine laboratory experiments (Osoba et al., 1951). However, for the flow of steam and water or for the general case of single-component two-phase flows these relations are not well known. To our knowledge, none of the relations that have been reported in the last few decades are known to be error free (Verma, 1986; Sanchez, 1987; Clossman and Vinegar, 1988). The main difficulties in these experiments, as we show later in this paper, have been due to inaccurate measurements of fluid saturations and inappropriate assignment of pressure gradients to individual phases.

Other techniques involving analysis of enthalpy transients from producing geothermal fields have been used to infer relative permeability relations (Grant, 1977; Sorey et al., 1980; Horne and Ramey, 1978). However these techniques do not eliminate all the variables and quite often the in-situ fluid saturations and the overall permeability structure (i.e matrix, fracture) are unknown. These curves are therefore approximations at best. As shown by the experiments reported by Osoba et al. (1951) and by Hassler (1944), laboratory measurements of relative permeability can still have error if capillary end-effects are not taken into account. The end-effects are known to cause pressure gradients and by extension saturation gradients resulting in a nonuniform distribution of fluids in the core particularly at low flow rates. Ignoring this effect may result in underestimating the relative permeability of the wetting phase and attributing a permeability value for the nonwetting phase to a wrong saturation (Verma, 1986). Though this type of error can be avoided for the two-phase, two-component flows under isothermal conditions, all of the experiments meant to determine steam and water relative permeability relations reported in the past have not been able to completely eliminate these errors for two main reasons: 1) measurements of fluid saturations are not easy since the phase change with pressure drop along the core implies that the material balance methods used in isothermal cases are inapplicable, and 2) the varying pressure gradients along the core due to the combined effect of the capillary end-effects and varying flowing fractions due to phase change generally imply that any average pressure gradient measurement across the core would be different from the actual gradients at points along the core. In the experiments reported here the errors discussed above have been reduced significantly by using X-ray computer tomography (CT) to measure fluid saturations and by using pressure gradients from zones with constant fluid saturations to compute the relative permeability relations.

In this work it was not possible to conduct the experiments under perfectly adiabatic conditions as the X-ray CT scanner imposes limits on the type of materials that can be used thus effectively eliminating the use of guard heaters. However, heat losses were minimized by using a thick layer of high performance insulation material. In addition heat losses from the core were measured at several locations using heat flux sensors. Numerical simulations were carried out to determine the optimum experimental conditions. This included determining the appropriate core length, the effect of heat losses and the time required for the onset of steady state conditions. In this paper, we begin by looking at the origins and the concept of relative permeability with a literature review. Following this our experimental apparatus and the method used are described together with the conditions that have to be met in order to overcome some of the errors associated with laboratory measurements. Next the results of the numerical investigations are discussed. Finally, we shall present the experimental investigations and a discussion of the results.

5.3 LITERATURE REVIEW

Relative permeability relations reported in the past have been from the two main sources: 1) Theoretical methods using either field data from well tests or production histories of the wells in producing fields, 2) Laboratory experiments performed by injecting either single or two-phase fluids through small cores or porous medium models.

Relative permeability relations derived from field data have generally been obtained by matching enthalpy data (Grant, 1977; Sorey et al., 1980; Horne and Ramey, 1978). In deriving these relations the reservoir is normally treated as a porous medium. The enthalpy is then determined as a function of in-situ fluid saturations which have to be estimated from the flowing fractions. These models suffer from a number of shortcomings due to the assumptions used. As discussed by Heiba et al. (1983), experiments are the most reliable method to determine relative permeability. However, laboratory techniques also suffer from limitations imposed by boundary effects caused by capillary forces. Capillarity introduces nonlinear effects on the pressure and saturation distribution of the wetting phase at the core exit. Thus experiments must be designed to eliminate these effects. Osaba et al. (1951) have given a summary of the methods used to obtain relative permeability for two-component systems that eliminate or minimize such effects and that have been used successfully in problems of oil and gas. Capillary pressure effects can be overcome by use of sufficiently long cores or by use of high injection rates (Osoba et al., 1951). Our experience shows that even conducting experiments at some rates referred to as high in published literature still leaves substantial end-effects. Thus taking pressure gradients across the core and averaging the saturation over the entire core still leads to errors in computing relative permeability. The second most common source of error has been in the determination of saturation. A number of

techniques have been reported, yet each can be shown to have difficulties of some kind when applied to steam-water flow.

One of the earliest attempts to measure relative permeability relations for single component two-phase flow was reported by Miller (1951). In these experiments liquid propane was injected into a core. Propane was allowed to flash as it moved across the core thus creating a two-phase flow with increasing gas fraction as the fluid moved further downstream. From the pressure and temperature measurements along the core and application of material and energy balance it was possible to determine the flowing fractions at each point and therefore to estimate the relative permeability relations. It is not clear whether capillary end-effects were adequately eliminated, and the calculated saturation could not be checked by other independent means.

Among the first attempts to measure saturations directly were those reported by Chen (1976) and Council (1979) using a capacitance probe method. In this technique, the saturation was obtained from a calibration based on the relation between the capacitance and the saturation within the core (Council, 1979). However the margin over which readings were obtained was small, thus leaving doubts on the reliability of the relative permeability relations obtained. Chen et al. (1978) recommended the use of a gamma-ray densitometer for measuring saturations. Later, Verma et al. (1985) and Verma (1986) used a gamma-ray densitometer for experiments using an artificial sand pack. Though this was an improvement over the capacitance probe, the portion of the sample accessed by the densitometer was small (5%). Problems with overheating of the equipment during the experiments resulted in only a small part of the relative permeability curve being investigated. In addition, fluid bypass between the core holder and the sand pack was suspected to contribute to the larger steam relative permeability obtained in the experiments.

Recently, Sanchez (1987) reported the use of average recovery time of a tracer injected with the fluid to determine the water saturation in the core. In these experiments, pressure was measured at only two points a short distance from the either end, effectively ignoring capillary end-effects. Sanchez (1987) estimated an average water saturation representing the whole core and ignored the variations in saturation expected from the capillary end-effects at low flow rates. In addition, the pressure drops reported by Sanchez (1987) over the interval of 50 cm are about 0.3 bars and phase change due to the pressure drop alone even in the absence of capillary end-effects would lead to a saturation gradient along the core. It is therefore possible to question the accuracy of these results.

Clossman and Vinegar (1988) are probably the first to report the use of X-ray CT scanner to measure water and steam saturations in porous materials. They investigated steam-water relative permeability in cores from oil fields at residual oil saturations. The cores used for the experiments were rather small i.e., 15.4 cm in maximum length and 2.47 cm in diameter. The flow rates were

also moderate, 3.31 cc/min to 20 cc/min. Steam quality was determined from two temperature measurements at the inlet and exit. The same readings were used to estimate heat losses from the core. Relative permeability relations were calculated from pressure measurement at the same points. Temperatures were not measured along the core but the distribution within the core was assumed to vary in three possible ways, linear, quadratic and constant. The core was enclosed in an aluminum sleeve kept under vacuum conditions to minimize heat losses. Clossman and Vinegar (1988) found that the relative permeability values for the steam phase were close to those reported by Brooks and Corey (1964) but those for the liquid phase were somewhat smaller. Though it is not clear how much each of the assumptions contributed to the final curves, Clossman and Vinegar (1988) did not investigate the influence of capillary end-effects which were bound to be significant due to the small core lengths and low flow rates they used. Secondly, it may be inaccurate to assume that the temperature within the core would vary in the manner assumed in their calculations. In two-phase systems, temperature and pressure are coupled by the Clausius-Clapeyron equation and depend on the capillary end-effects, giving rise to temperature variations that are highly nonlinear and not quadratic.

More recently Piquemal (1994) has reported relative permeability relations for steam and water using methods similar to those used by Verma (1986). The porous medium was an unconsolidated material packed in a tube 25 cm long and with an internal radius of 5 cm. Pressure and temperature were measured at four points 5 cm apart along the core holder. The injection rates were changed from 10^{4} to 10^{-3} kg/s (6.0 to 60.0 gm/min). The experiments were conducted at 180 ^{o}C. Though Piquemal (1994) did not discuss any errors in his measurements, the experiments were subject to the same problems reported by Verma (1986) who used a similar apparatus. The problems include limitations on saturation measurement by the gamma-ray densitometer and steam by-pass between the porous medium and the core holder. It is important to notice that the results reported by Piquemal (1994) are different from those obtained by Verma (1986) who observed enhanced permeability of the steam phase. Piquemal (1994) obtained results suggesting that steam-water flows are similar to nitrogen-water.

This review shows that there is a wide range of results that have been reported, some of which even used similar experimental apparatus. The main reason for this has been the difficulties in measuring saturations accurately and using incorrect pressure gradients to compute relative permeability. The investigations reported in this paper overcame these difficulties by using the X-ray CT scanner to measure saturation accurately and by evaluating pressure gradients actually within the zones of constant saturation only.

5.4 EXPERIMENTAL APPARATUS AND PROCEDURE

The description of the apparatus for these experiments was discussed in Satik et al. (1995) and Ambusso (1996). In general, it consists of an injection unit, and a core holder made of epoxy. The injection unit consisted of two furnaces to generate steam and hot water. Two temperature controllers were used to control the temperatures of the two furnaces. Temperatures were measured by the thermocouples inserted in ceramic protection tubes embedded within the outer most layer of the epoxy core holder. A 12-channel thermometer unit was connected to a computer for storing and displaying the temperature data. The thermometer gathered readings from the eleven J-type thermocouples, eight of which were located on the core while the other three were on the steam line, the water line and the mixing point for the steam and water at the injection end of the core. Pressures were measured by using eleven pressure transducers each with its own read-out screen. Some of the transducers were also connected to chart recorders. Direct monitoring of pressures and temperatures during the experiment enabled us to determine when steady state conditions had been reached. Heat losses on the core body were measured by using heat flux sensors placed at various locations along the core body.

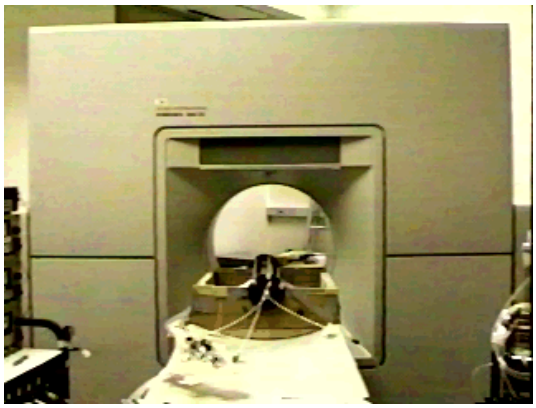

(a)

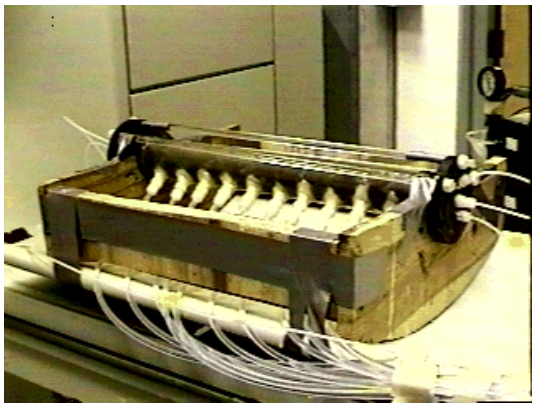

(b)

Figure 52: Pictures of (a) X-ray CT scanner and (b) the core holder used in the flow experiments

The core (rock) samples used for these experiments have been described in detail in Ambusso (1996) and had the following properties; permeability 600md, porosity 20%, length of 38 cm and diameter of 5.04 cm. The core sample was first heated to 450°C for twelve hours to deactivate clays and to get rid of residual water. The two ends of the core were then covered by the end plugs fitted with nipples for injection and production of fluid. Eight ports to measure temperatures and pressures were then fitted at the fixed intervals along the edge of the core before the rest of the core was covered completely by high temperature epoxy. The core was tested for leaks before being covered with an insulation material made of ceramic blanket. The core was placed on a motorized bench that could be moved to precise locations and scanned as required. A picture of the experimental apparatus within the X-ray CT scanner is shown in Figure 52.

Saturations were measured by using a high resolution X-ray CT scanner. As a requirement, however, high density materials such as most metals or large pieces of intermediate density materials like some forms of plastics could not be placed in the area being scanned since they are almost opaque to X-rays. This imposed a severe restriction on the types of materials that could be used for constructing the core holder. A review of previously published literature did not reveal a core holder without any major metal parts that had been used for this type of experiment. Several investigators (e.g. Closmann and Vinegar, 1988) have reported using core holders made of aluminum materials. They however used X-rays at higher energy levels than our X-ray CT scanner equipment could handle. This ruled out the use of similar designs for the experiments. The first step therefore was to design and construct a core holder that could be used in the CT scanner and that could also withstand high temperatures and pressures for extended periods of time. In addition, the issues associated with minimizing heat losses had to be resolved since guard heaters, which have been used previously in similar experiments, could not be used (Verma, 1986; Sanchez., 1987). Several attempts were made to ultimately design such a core holder, as described in more detail by Ambusso (1996).

The experimental procedure was as follows. First, air inside the pore space was displaced out by injecting several pore volumes of CO_2 then the core was scanned at predetermined locations to obtain dry-core CT (CT_{dry}) values. Next, water was injected into the core to remove CO_2 and to eventually saturate it completely. This step continued until the core was completely saturated with water, at which time the core was X-ray scanned again at the same locations to obtain wet-core CT (CT_{wet}) values and, pressure and temperature readings were taken at this time. Steady-state relative permeability experiments involve injection of varying fractions of steam and water, at a constant total flow rate, into the core. Measurements done at each step result in a single data point on relative permeability vs. saturation curve. Starting from completely water saturated core and injecting steam at increasing fractions will give rise to a drainage process while the opposite procedure gives rise to an imbibition process. Each step continued until steady-state conditions at which injection and production rates became the same for both steam and water and also pressures

and temperatures stabilized. At the onset of steady-state conditions, another X-ray scanning was done along the core at the same locations to obtain CT (CT_{exp}) values corresponding to the particular steam-water fraction. Next, the steam-water fraction was changed, keeping total flow rate constant, and the above procedure was repeated.

After the experiment was completed, an interpretation software was used to calculate the porosity and saturation distributions from the CT values obtained with the scanner. To calculate porosity the following expression was used:

$$\phi = \frac{CT_{wet} - CT_{dry}}{CT_{water} - CT_{air}} \tag{9}$$

where CT_{water}, CT_{air} are CT numbers for water and air, respectively. Similarly, the expression used to calculate saturations is:

$$S_{st} = \frac{CT_{wet} - CT_{\exp}}{CT_{wet} - CT_{dry}} \tag{10}$$

and

$$S_w = 1 - S_{st} \tag{11}$$

where S_{st} and S_w denote steam and water saturations, respectively.

5.5 NUMERICAL RESULTS

Prior to the experiments, numerical simulations were carried out to determine the optimum dimensions of the core required to overcome capillary end-effects and to evaluate the effect of injection rates and steam fractions on the results. The effects of heat losses on the temperature, pressure and saturation measurements were also evaluated. In addition, the numerical simulations were used to estimate the time required for the experiments to reach steady state conditions. These simulations were described in Ambusso et al. (1996).

The STARS software was used for the numerical investigation. This program is a multicomponent thermal simulator specifically designed to handle heavy oil operations such as surfactant flooding, steam injection and in-situ combustion in single and dual porosity media, and fractured reservoirs. Three main aspects were investigated; the effect of the type of relative permeability curves, the effect of flow rates and flowing fractions on pressure, temperature and saturation and the effect of heat losses on fluid distribution along the core and fluid segregation due to the combined effects of gravity and condensation. Several methods of investigation were used. In all of the cases the physical dimensions of the models were similar to those used for the experiments (a core of 5.08 cm in diameter and 43.2 cm in length). Permeability and porosity values were set to 600 md and 20%, respectively. The injection and production points were fixed at the centers of the end plates. In each simulation run, the parameters of interest were saturation, pressure and temperature.

Three types of relative permeability curves were used in the numerical simulations: the widely used Corey (1954), the linear curves and the curves derived by Verma (1986). These curves are shown in Figure 53. In particular, the curves reported by Verma

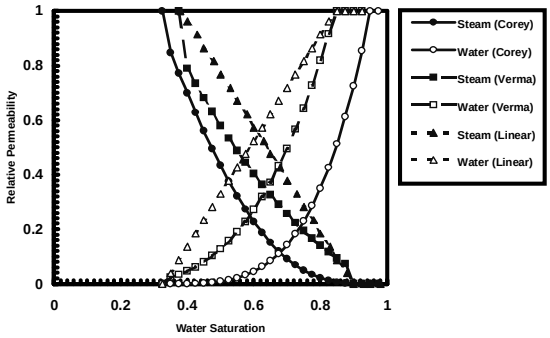

Figure 53: Relative permeability curves used for the numerical simulation.

(1986) were of interest since these curves represent a more recent measurement and the methods used to obtain them were similar to ours. In order to reduce the number of variables between the curves the irreducible saturations for the liquid phase from the curves obtained by Verma (1986) were used for all of the curves.

In order to reproduce the end-effects it was necessary to incorporate a capillary pressure in the simulator. These functions are well known for oil and water under static conditions. In the case of steam-water flow in porous media, however, these functions are currently not known. We therefore used the relations for water and nitrogen given in a parametric form $-C*ln(Sw)$ (Aziz, 1995), where C is a constant. To mimic the capillary end-effects, the core was divided into several small blocks. The first and the last blocks were assigned zero capillary pressure. In real situations the capillary pressure may be small but will always be non-zero in the injection lines.

Figure 54 shows the numerical simulation results of saturation distributions obtained using different relative permeability curves. The total injection rate is 14 cc/min of water and the steam quality is 0.1. In all of the cases the flow was modeled as adiabatic. It is clear that the linear relative permeability curves predict lower steam saturations. They also give lower pressure drops across the core for all of the injection rates. This is consistent with the higher mobility predicted (equal to unity for all saturations) for the combined flow steam and water. In all of the cases the steam saturation increases marginally towards the production end until the end-effects reverses the trend. This, too, is consistent with the flashing of water into steam as the pressure declines. In all of the cases, the capillary end-effects are very strongly expressed but decrease as flow rate increases. The results also show that it is possible to have a substantial flat saturation profile even for modest

injection rates. These curves suggest clearly that the type of relative permeability curve has a significant influence on the results obtained.

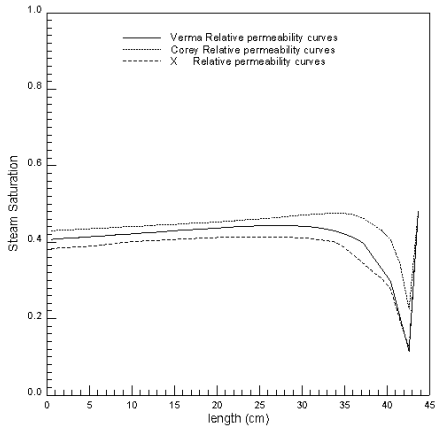

Figure 54: Saturation distribution for different relative permeability relations.

To investigate the effect of flow rate, the relative permeability curves obtained by Verma (1986) were used. In each case the steam quality (in mass) was kept constant at 0.05. The injection rates were 8, 15 and 20 cc/min. Figure 55 shows the numerical simulation results of saturation distributions at these three flow rates. These results show the expected behavior. The portion of the curve affected by the capillary end-effects decreases as the flow rate increases. The pressure and temperature also rise to higher values as the flow rate increases. These results show that the appropriate length for the core which is not to be affected by end-effects is about 30 cm. Therefore a core length of 43.2 cm was selected to be used for the experiments.

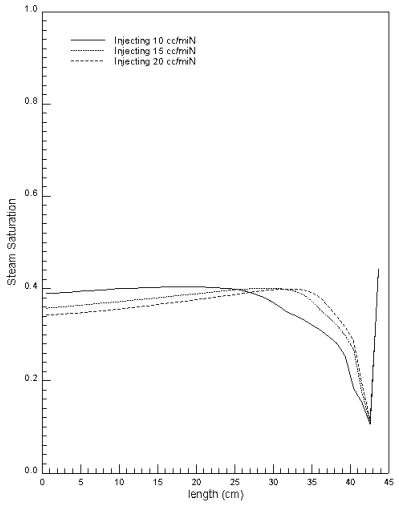

Figure 55: Saturation distributions for three different injection rates, obtained from the numerical simulation.

To investigate the effect of heat loses on fluid segregation, a three-dimensional numerical model was constructed by dividing the core into a 100x3x3 grid in the x, y and z directions, respectively. Insulation around the core was added as an additional layer of low thermal conductivity in the y, and z directions. The thickness of the insulation was set to 2.54 cm and the porosity and permeability of the insulation were set to zero. In the simulator, the thermal properties were set to those provided by the manufacturer. The curves obtained by Verma (1986) and a flow rate of 12 cc/min were used to generate the results shown in Figure 56. The results are for the middle three layers from the uppermost to the lowest. As expected, the temperature and pressure are practically the same for all of the blocks at a given cross-section except at the end blocks where there exists a non-axial flow. Saturations vary only marginally in the vertical direction.

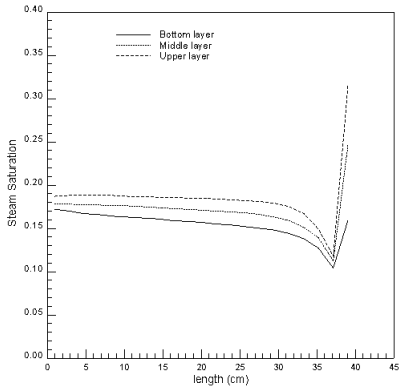

Figure 56: Saturation distributions for three vertical layers, obtained from the numerical simulation.

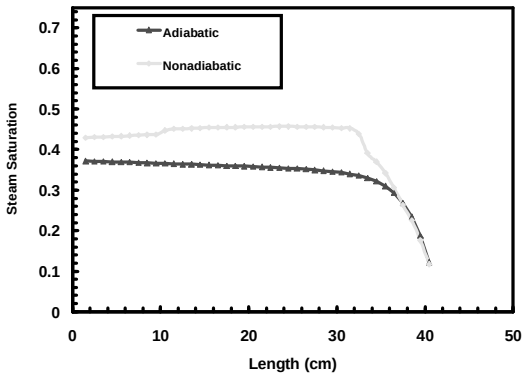

Figure 57: Saturation profiles for adiabatic and non-adiabatic cases, obtained from the numerical simulation.

To compare the results obtained with and without heat losses a one-dimensional model was constructed with the same dimensions. The comparison of results from these two models is shown on Figure 57. There still is a flat saturation profile over the most of the early part of the curve but

the capillary end-effects are more strongly expressed and start earlier for the non-adiabatic case. Also, the steam saturation does not show the marginal increase observed for the adiabatic cases but is rather simply flat. This is an important aspect of these results since only one value of saturation was computed per section, effectively making the experiments one-dimensional. Recognition of the variation in saturation was an important confirmation of acceptable results. This indeed was the case. These results indicate that heat losses will affect the measurements but the main features will be unaffected. Thus a flat saturation profile, which is required to evaluate relative permeability accurately, is still present and is of sufficient length.

5.6 EXPERIMENTAL RESULTS

The single core dynamic method was used for the measurement of the relative permeability. This method required that a two-phase mixture of steam and water be injected into the core. By changing the flowing fractions of each phase and letting the system adjust itself to steady-state conditions, the relative permeability relations were determined from the knowledge of the flowing fractions and the measured pressures and temperatures. To determine the flowing fractions it is necessary that the enthalpy of the injected fluid be known accurately. Thus it is important that the injected fractions of the components in the core be known before injection and the phase change accompanying pressure drop be considered. Though it has been suggested that in the porous media the process of boiling and phase change may require more energy due to capillary forces (Udell, 1982), experiments by Miller (1951) with light gasoline showed that the temperature and pressure follow values close to those for flat surface thermodynamics. For this reason steam table values were used to compute flowing phase proportions in the core.

We used two methods to inject fluids of known enthalpy. The first was to inject a two-phase mixture that was heated to high temperature but always keeping the pressure above saturation so that the fluid always remained in the liquid phase upstream of a throttle valve set to release fluid only after some threshold pressure has been reached. The enthalpy of the two-phase mixture would be the same as that of the liquid water corrected for heat losses along the line, the kinetic energy being negligible in this case. This method is a modification of that used by Miller (1951) and Arihara (1976) who injected the fluid as a single phase into the core. For these experiments this method was used for injection of fluid at low enthalpy to obtain relatively low steam fractions and proved useful since steam table values could be used to determine the enthalpy given either the temperature or the pressure. The second method was to mix streams of steam and water. Due to difficulty in keeping both streams close to saturation, steam was superheated by a few degrees and liquid water was kept a few degrees below the boiling point. This too enabled the use of steam table values for computation of the phase fractions. This approach was used to obtain high steam fractions.

After assembling the core and the auxiliaries, the experiment was initiated by first determining the porosity of the core. This was done by taking X-ray CT scans of the core at various locations when it was dry and again when it was fully saturated with water. First, a steady stream of carbon dioxide was passed through the core for several hours and the initial scan, referred to as the *dry scan*, was performed to obtain CT_{dry} values. Following this, a steady stream of water at low flow rate (5 cc/min) for sufficiently long time (12 hours) to saturate the core completely with water. A second scan, referred to as the *wet scan*, was then conducted to obtain CT_{wet} values at the same locations as the *dry scan* was performed. By using Equation9 and these two sets of images obtained at every point scanned it was possible to determine the porosity distribution of the core. The average porosity was found to be about 20%. These scans also revealed that the core had a few vugs identified as points with higher porosity from the bar scale. After the porosity distribution had been determined the absolute permeability was determined by flowing water at different flow rates and measuring pressures along the core. Three rates were used and the results are summarized in the Table6. The results were taken after an hour of injection. The readings show that there is a small dependence of permeability on injection rate.

After determining the absolute permeability, the core was brought to experimental conditions by injecting hot water. Increasing the temperature of the water was done in stages to avoid problems of rapid thermal expansion and shock. These heating stages at low flow rates provided an additional opportunity to check the permeability of the core at higher temperatures. The permeability values at higher temperatures were found to be within the range of those measured at the room temperature, giving credence to the assumption that permeability does not change with temperature.

Table 6: Permeability measured at different injection rates.

Rate cc/min	Pressure psig	Pressure psig	Permeability md
10	7.8	6.5	944
15	10.2	8.5	1082
20	13.1	10.8	1102

Once the target temperature for the experiments had been reached, the core was allowed to attain thermal equilibrium before any readings were taken. During the experiment the phase fractions of the injected fluids were changed 14 times while attempting to increase the steam fraction (and steam saturation in the core). Each of these 14 attempts will be referred as steps in this description. For the first four steps only the water line was used. The steam fraction was adjusted by changing the injection temperature and the flow rate. For the subsequent five steps both the steam and water lines were used. In practice, controlling injection temperature and steam fractions was a very

difficult task since the steam generators took too much time to reach thermal equilibrium each time the flow rate or temperature was changed. As a result the steam fractions being injected were initially either less or more than intended and slowly stabilized at the correct values. The same problem was also encountered when water flow rate was changed.

Steady-state conditions were recognized by the stabilization of temperature and pressure. Typically stabilization took three to five hours, though the measurements reported here were taken after at least eight hours. Once a steady state had been confirmed, the measurements of temperature and pressure were recorded together with the heat flux sensors readings. The X-ray CT scans were then taken at locations where the dry and wet scans had been taken to obtain CT_{exp} values. These scans were then processed into saturation images using Equations 10 and 11. The saturation profiles presented in this paper were obtained by averaging the saturation values over a cross sectional area of the core. To determine whether the distribution was uniform each image had to be examined. In general the images showed very uniform saturations for most sections for all flow rates.

In general all of the images gave an average porosity of 20±0.5%. In spite of this uniform value some images had regions of local variations in porosity. Figure 58 shows the porosity distributions obtained from the X-ray CT scanning at four locations along the core. Some of the images show zones with somewhat different porosity. It is not clear whether the anomalous zones are due to larger pores or due to a different packing of sand grains. Otherwise, the porosity over the most of the core length is very close to the average porosity. This core can therefore be considered a close approximation to a uniform porous medium.

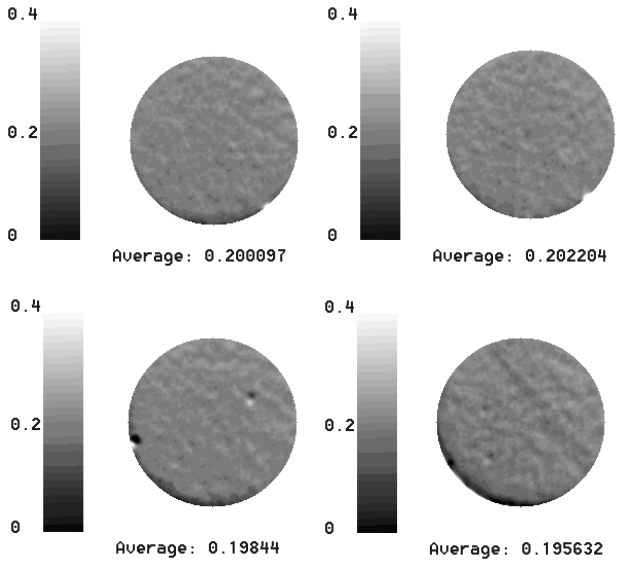

Figure 58: Selected images for porosity distributions obtained from the X-ray CT scan.

Figure 59 shows all of the saturation profiles obtained during the experiments. In general all of the saturation profiles show a decreasing trend from the injection end to the production end which was also observed in the numerical simulation results for the non-adiabatic case. The first and second steps of injection show a few irregular trends at 17 cm and at 25 cm from the injection point. These trends are also repeated to a lesser degree at the same points at higher saturations. These anomalies are attributed to the inhomogeneities existing in permeability or porosity. These are however minor and the saturations still reflect the general trend. In addition, the values of saturation are never really constant but change gradually. Thus the flat saturation profiles are not always "flat". However the values change very little over the most of the core length and can be averaged over an interval to a representative value. In addition, from previous experience with other experiments (e.g. oil and water) relative permeability typically changes monotonically with saturation by small amounts. Therefore, relative permeability computed over regions where saturations vary by less than ±2 % can be considered to be constant. The saturation profiles shown in Figure 59 reveal a number of other interesting features. The capillary end-effects are observed at low steam flow rates with high steam fraction. This can be seen for steps that are different in rates but have the same steam fractions (e.g. Steps 4 and 5). This supports some of the results obtained from the simulation where the end-effect is very strong at small flow rates.

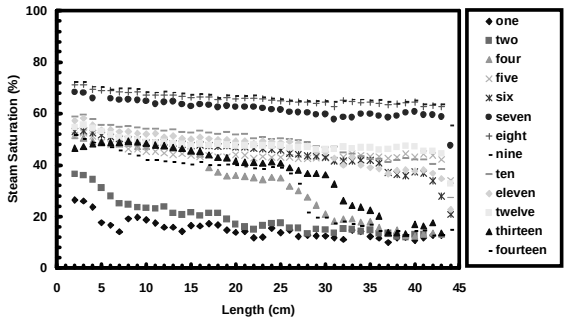

Figure 59: Saturation profiles for all of the steps conducted during the experiment.

Figures 60 and 61 show steady-state temperature and pressure profiles, respectively. As described in the experimental apparatus section, the thermocouples were inserted in ceramic tubes within the outer most layer of the epoxy. Thus the thermocouples probably did not make direct contact with the core. This might have led to lower temperature readings than expected. The pressure readings were taken using teflon tubes attached on the core body. To ensure that the readings were for the water phase these tubes were filled completely with water. By this method water in the tubes was assumed to be in contact with water in the core. In general all of the pressure measurements reflected the expected behavior i.e. decreasing values along the core from the injection end. The values were read by pressure transducers which had a minimum scale division of 1 psi. The error

was therefore about 0.5 psi. This value was taken into account when computing the relative permeability.

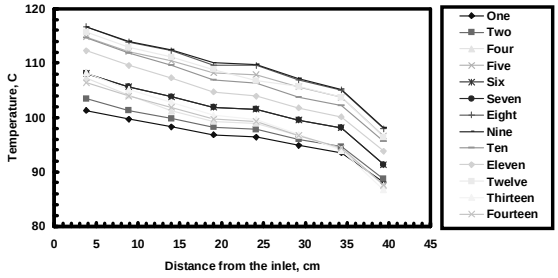

Figure 60: Temperature profiles for all of the steps conducted during the experiment.

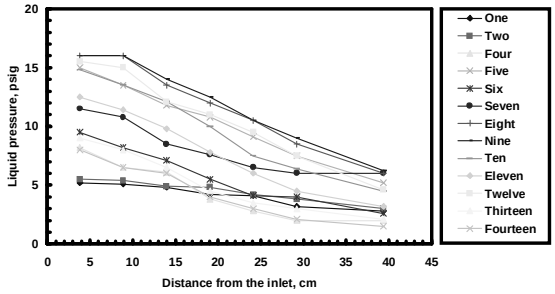

Figure 61: Pressure profiles for all of the steps conducted during the experiment.

Since it was not possible to use guard heaters the experiments were not conducted under perfect adiabatic conditions. Thus the interpretation of the results must take heat losses into considerations. This requires that the heat lost through the system be accounted for and the flowing fractions corrected accordingly. Heat losses were measured only on the body of the core. In the steam and water line, the heat losses were estimated by recording the temperature drop while flowing a known amount of fluid. Since the heat loss rate is only governed by the temperature difference between the material being considered and the surrounding, these results could be extended to the case of any other fluid under similar conditions. This was done to estimate the heat lost from the injection lines before and after the mixing of fluids.

The starting point of this derivation are the conservation equations for mass and energy fluxes:

$$m_t = m_v + m_l \tag{12}$$

$$m_t h_t = m_v h_v + m_l h_l + Q \tag{13}$$

where m and h refer to mass flow rate and enthalpy, respectively and the subscript t refers to total, v to vapor phase and l to the liquid phase. Q is the total heat lost upstream of the point being considered.

Then using flat interface thermodynamics the steam fraction x() in the flow at any time would be given by:

$$x = \frac{m_t (h_t - h_l) - Q}{m_t h_{lv}} \tag{14}$$

h_{lv} is the latent heat of vaporization at the prevailing temperature and pressure.

Then the relative permeabilities to steam and water can be calculated by the corresponding Darcy's equations for each phase in terms of the mass flow rates:

$$k_{rl} = -\frac{(1-x) m_t \mu_l \nu_l}{kA \frac{\Delta p}{\Delta x}} \tag{15}$$

and

$$k_{rs} = -\frac{x m_t \mu_s \nu_s}{kA \frac{\Delta p}{\Delta x}} \tag{16}$$

Thus a knowledge of the values of flowing mass fractions in the above equations and pressure drop along a column of the core with constant or flat saturation provides a value for the relative permeability.

Critical to the evaluation of the flowing fractions is the knowledge of the injected enthalpy and the heat losses. Table 7 shows the heat losses on the core body which were computed from the measurement of the heat flux directly. Determining heat losses along the injection lines were however a major challenge. They were estimated from the temperature drop while injecting water during the heating process. In Table8, we show the heat loss rate calculated from the product of the mass flow rate and the enthalpy difference corresponding to the temperature drop between the back-pressure valve and the mixing point. The values lie on a straight line when plotted which lends credibility to the approach. These heat loss values, though high, represented less than 5% of the total for high flow rates and were twice this for low flow rates.

To determine the flowing fractions at a particular point, the heat losses upstream of the point under consideration was evaluated and subtracted from the total energy at the injection point. The heat lost in the injection line was estimated from the plot of heat loss rate vs. injection temperature, obtained using the values given in Table8 (Ambusso, 1996). The second component was the heat lost on the core before the fluid reached the point under consideration. This could be estimated from the heat flux sensor measurements which indicated how much heat was being lost in the radial direction. In the direction of flow, the temperature gradient also leads to conductive heat transfer. This component is small compared to heat lost in the radial direction and was neglected in the computations.

Table 7: Heat loss rate obtained from the heat flux sensors.

	Heat Loss Rate, kW/m^2			
Step	Sensor 1	Sensor 2	Sensor 3	Sensor 4
2	0.37634	0.1209	0.109663	0.111083
4	0.378717	0.147147	0.126428	0.11005
5	0.379233	0.148283	0.124775	0.110567
6	0.387138	0.148283	0.124775	0.110567
7	0.402225	0.138725	0.107028	0.135573
8	0.417157	0.15345	0.140017	0.118833
9	0.417157	0.167759	0.130302	0.133016
10	0.408632	0.160167	0.133636	0.127078
11	0.400158	0.163525	0.140482	0.140998
12	0.407908	0.162233	0.140017	0.142342
13	0.385433	0.1581	0.137433	0.124
14	0.380267	0.151383	0.128392	0.113925

Table 8: Heat loss along the injection line.

Flow Rate cc/min	T_{upst} ^oC	T_{downst} ^oC	Enthalphy Change, kJ/kg	Heat Loss, W
10	58.4	55.8	10.882	1.81367
10	68.3	64.9	14.246	2.37433
10	100.9	94.6	26.601	4.4335
15	105.9	102.1	20.266	5.0665

To use the heat losses from the heat flux sensors, it was found convenient to convert the heat flux sensor readings into graphs that gave the cumulative heat lost as the fluid moved along the core. This was done for each set of measurements. Thus to compute the flowing fractions, Equation 14 was used after Q had been calculated from the summation of the heat lost on the body and the heat lost along the injection line. These were then converted into volumetric flow rates for the prevailing temperature and pressure. Since the pressure and therefore the specific volume of steam changed along the core, the volumetric flow rate was computed for all the points along the core and the average value over the interval used. The volumetric flow rates were surprisingly similar and generally did not differ by more than 2% over 5 cm intervals.

The next parameter of interest was the temperature dependent viscosity particularly for water which varied between 252 and 211 x 10^6 kg/m-s. The arithmetic mean of the values at the two end points was used for a given interval. A final correction to the results was to include the errors due to pressure measurements. This was done for all the intervals. The error assumed in each case was ±0.5 psi. Table 9 shows a summary of the essential data from all of the steps conducted during the experiment. The relative permeability values computed from the experimental data are plotted on Figure 62. The relative permeability for the steam and water phases vary approximately linearly with saturation. In view of the common usage of so-called "X curves" in numerical simulations, this is a rather fortunate result.

Table 9: Summary of important results.

Step	q_{water}, cc/min	q_{steam}, cc/min	S_{st} %	k_{rw}	k_{rs}
1	15	0	15-10	0.84658	0
2	13.6	414.6	22	0.781885	0.091682
4	7.78	274	38	0.337338	0.521257
5	7.82	1062	50	0.305915	0.747689
6	3.46	625.7	53	0.209797	0.657116
7	3.49	762.6	64	0.086876	0.839187
8	0.16	1007.8	68	0.024954	0.9122
9	0.19	1007.7	68	0.031423	0.900185
10	4.052	883.8	63-54	0.151571	0.695009
11	4.31	708	52-49	0.182994	0.72366
12	5.82	559.7	49	0.202403	0.680222
13	5.77	436.5	45-39	0.28281	0.608133
14	7.73	893.8	43	0.365989	0.507394

5.7 CONCLUSION

The relative permeability curves presented in this paper have been derived from experiments in which the saturations within the core have been measured by using an X-ray CT scanner. Furthermore the saturation profiles have been shown to follow very closely what is expected from the numerical simulation. The residual limits are not well defined in the experiments, because it was not possible to inject steam at 100% quality due to condensation in the injection line. It was also not possible to estimate the steam relative permeability at low saturations as the correction for the enthalpy of the injected fluid was very close to the correction in heat lost from the injection line and the core body. These end points are however inferred from the relative permeability curves and are about 20% for the water and less than 10% for the steam phase.

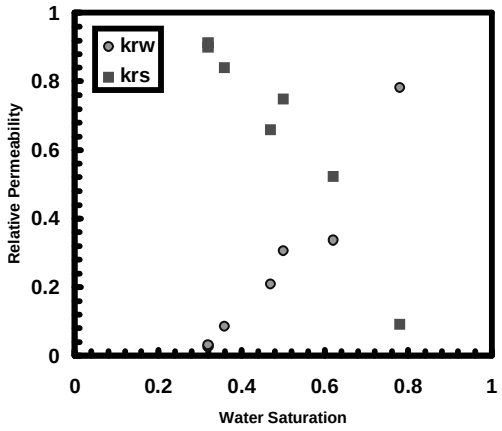

Figure 62: Relative permeability for steam and water.

Several relative permeability relations for flow of steam and water in porous media derived from experiments have been proposed in the past (Chen et al., 1978; Council and Ramey, 1979; Verma, 1986; Clossman and Vinegar, 1988). In all of the curves reported in the past the relative permeability for one or more of the phases have tended to follow the relations obtained by Corey (1954) for nitrogen and water. However none of the previous investigators have measured saturation directly in the manner of the experiments reported here. As a result, none of them has measured the pressure of a single phase alone over any interval. Unlike previous investigations, these results show that the relative permeability for both phases are enhanced in comparison to relations obtained by Corey (1954).

The principal feature of the measured relative permeability curves is their close similarity to the so-called “X curves”. Use of the “X curves” for geothermal simulation has been common, but until now has been based only on philosophical arguments.

6. REFERENCES

Ambusso, W.J., "Experimental Determination of Steam-Water Relative Permeability Relations", MS Thesis, Stanford University, Stanford. CA 1996.

Ambusso, W.J., Satik, C. and Horne, R.N., "A Study of Relative Permeability For Steam-Water Flow in Porous Media", *Proc.* 21st Stanford Workshop on Geothermal Reservoir Engineering, 1996.

Arihara, N., "A Study of Non-Isothermal Single and Two-Phase Flow Through Consolidated Sandstones", PhD dissertation, Stanford University, Stanford. CA, 1976.

Bailey, E.H., Irwin, W.P., and Jones, D. (1964), "Franciscan and Related Rocks, and their Significance in the Geology of Western California", California Division of Mines and Geology, Bulletin 183, 141p.

Blake, M.C. ,Jr., Irwin, W.P., and Coleman, R.G. (1967), "Upside-down Metamorphic Zonation, Blueschist Facies along a Regional Thrust in California and Oregon, U.S.", Geological Survey Professional Paper 575-C, pp. C-1 through C-9.

Brooks, R.H. and Corey, A.T., "Hydraulic Properties of Porous Media", Colorado State University, Hydro paper No.5, 1964.

Chen, H.K., "Measurement of Water Content in Porous Media Under Geothermal Fluid Flow Conditions", Ph. D. Thesis, Stanford University, Stanford, California 1976.

Chen, H.K., Council, J.R., and Ramey, H.J., Jr., "Experimental Steam-Water Permeability Curves", GRC *Trans*. Vol. 2, 1978, pp 102-104.

Clossman, P.J. and Vinegar, H.J., "Relative Permeability to Steam and Water at Residual Oil in Natural Cores; CT Scan Saturation", SPE Paper 174449, 1988.

Corey, A.T., "The Interrelations Between Gas and Oil Relative Permeabilities", *Producers Monthly* Vol. 19 1954. pp 38-41.

Correa, A.C., and Ramey, H.J., Jr. (1994): "Theoretical Investigation of Adsorption in Porous Media", submitted for publication in Society of Petroleum Engineers Advanced Technology Series.

Counsil, J.R., “Steam-Water Relative Permeability”, Ph. D. Thesis, Stanford University, Stanford, California, 1979.

Counsil, J.R., and Ramey, H.J., Jr., “Drainage Relative Permeabilities Obtained From Steam Water Boiling Flow and External Gas Drive Experiments”, GRC*Trans*. Vol. 3 1979, pp 141-143.

Economides, M.J., and Miller F.G. (1985): "The Effects of Adsorption Phenomena in the Evaluation of Vapor-Dominated Geothermal Reservoirs", *Geothermics*, vol. 14(1), pp. 3-27.

Enedy, S., Enedy, K., and Maney, J. (1992): "Reservoir Response to Injection in the Southeast Geysers", *Monograph on the Geysers Geothermal Fields*, C. Stone (ed.), Geothermal Resources Council, pp. 211-219.

Fulcher, R.A. Jr., Ertekin T. and Stahl, C.D., “The Effects of Capillary Number and Its Constituents on Two-Phase Permeability Curves”, SPE Paper 12170, 1983.

GRC Special Report 17 (1992), Monograph on The Geysers Geothermal Field, Geothermal Resources Council, Special Report 17.

Grant M.A., “Permeability Reduction Factors at Wairakei”, Paper presented at AIChE-ASME Heat Transfer Conference, Salt Lake City, Utah, August 1977, pp 15-17.

Harr, M.S. (1991): "*Laboratory Measurements of Sorption in Porous Media*", MS Report, Stanford University, August 1991.

Hassler, G.L., “Method and Apparatus for Permeability Measurements”, U.S. Pat. Off., Washington, D.C., 1944.

Heiba, A.A., Davis, H.T. and Scriven, L.E., “Effect of Wettability on Two-Phase Relative Permeabilities and Capillary Pressure”, SPE paper 12172, 1983.

Hebein, J.J. (1986), “Conceptual Schematic Geologic Cross-Sections of The Geysers Steam Field”, Proceedings of the Eleventh Annual Geothermal Engineering Workshop, Stanford University, pp. 251-258.

Herkelrath, W.N., Moench, A.F., and O'Neal, C.F., II (1983): "Laboratory Investigation of Steam Flow in a Porous Medium", *Water Resources Research*, vol. 19(4), pp. 931-937.

Herkelrath, W.N., and O'Neal, C.F., II (1985): "Water Vapor Adsorption in Low-Permeability Rocks", International Association of Hydrogeologists, (ed.) Memories, Vol. XVII, Part I, pp. 248-253.

Holt, R., and Pingol, A., "Adding Adsorption to a Geothermal Simulator", Proc. of the 17th Annual Workshop on Geothermal Reservoir Engineering, Stanford University, California, January 1992.

Hornbrook, J.W. (1994): "The Effects of Adsorption on Injection into and Production from Vapor Dominated Geothermal Reservoirs", PhD thesis, Stanford University, January 1994.

Horne R.N., and Ramey H.J. Jr., "Steam/Water Relative Permeabilities From Production Data", GRC *Trans*. Vol. 2 1978, pp 291.

Horne, R.N., Ramey, H.J. Jr., Shang, S.B., Correa, A.C., and Hornbrook, J.W., "The Effects of Adsorption and Desorption on Production and Reinjection in Vapor-Dominated Geothermal Fields", Proc. of the World Geothermal Congress 1995, Florence, Italy, May 1995, pp. 1973-77.

Hsieh, C. H. (1980): "*Vapor Pressure Lowering in Porous Media*", PhD Thesis, Stanford University.

Hsieh, C. H., and Ramey, H.J., Jr. (1983): "Vapor-Pressure Lowering in Geothermal Systems", *SPEJ*, vol. 23(1), pp. 157--167.

Hulen, J., Walters, M. and Nielson, D. (1991), "Comparison of Reservoir and Caprock Core from the Northwest Geysers Steam Field, CA-Implication for Development of Reservoir Porosity", Geothermal Resources Council Transactions, Vol.**15**, pp. 11-18.

Hulen, J. B. and Walters, M. (1994), "The Geysers Felsite and associated Geothermal Systems, Alteration, Mineralization, and Hydrocarbon Occurances", in: Active Geothermal Systems and Gold-Mercury Deposits in the Sonoma-Clear Lake Volcanic Fields, CA (J.J. Rytuba, ed.), Guidebook Series, Soc. Economic Geologists, vol.16, pp. 141-152.

Hulen, J. B. and Nielson, D. C. (1995), "The Nature of Faults and Hydrothermal Veins in Corehole SB-15D, The Geysers Steam Field, CA", GRC Transactions, Vol.**19**, pp. 181-188.

Leutkehans, J. (1988): "*A Laboratory Investigation of Steam Adsorption in Geothermal Reservoir Rocks*", MS report, Stanford University.

Lim, K-T., “Simulation of Fractured Reservoir with Sorption and Applications to Geothermal Reservoir”, PhD thesis, Stanford University, California, March 1995.

Lovekin, J., and Horne, R.N.: "Optimization of Injection Scheduling in Geothermal Fields," G.R.C. *Transactions*, 11, 1987.

McLaughlin, R.J. (1981), “Tectonic Setting of Pre-Tertiary Rocks and Its Relation to the Geothermal Resources in The Geysers-Clear Lake Area”, U.S. Geological Survey Professional Paper 1141, pp. 3-23.

McLaughlin, R.J. and Donnelly-Nolan, J. M. (Editors) (1981), “Research in the Geysers-Clear Lake Geothermal Area, Northern CA”, U.S. Geological Survey, Professional Paper 1141, 259p.

Miller, F.J., “Steady Flow of Two-Phase Single-Component Fluids Through Porous Media”, *Trans*. AIME, **192**, 1951, 205.

Osoba, J.S., Richardson, J.J., Kerver, J.K., Hafford J.A., and Blair, P.M., “Laboratory Measurements of Relative Permeability”,*Transactions*, AIME, Vol.**192**, 1951, pp. 47-55.

Piquemal, J., “Saturated Steam Relative Permeabilities of Unconsolidated Porous Media”, *Transport in Porous Media* **17**, 1994. pp 105-120.

Pruess, K., and O’Sullivan M., “Effects of Capillarity and Vapor Adsorption in the Depletion of Vapor-Dominated Geothermal Reservoirs”, Proc. of the 17th Annual Workshop on Geothermal Reservoir Engineering, Stanford University, California, January 1992.

Pruess, K., “Numerical Simulation of Water Injection into Vapor-Dominated Reservoirs”, Proc. of the World Geothermal Congress 1995, Florence, Italy, May 1995, pp. 1673-79.

Ramey, H.J., Jr. (1990): "Adsorption in Vapor-Dominated Systems",*DOE Geothermal Program Review* VIII, San Francisco, CA, pp. 63-67.

Ruthven, D.M. (1984): "*Principles of Adsorption and Adsorption Processes*", Wiley, New York.

Sanchez, J.M., “Surfactant Effects on the two-Phase Flow of Steam/Water and Nitrogen/Water in an Unconsolidated Permeable Medium”, Ph. D. Thesis, University of Texas, Austin, Texas, 1987.

Sta.Maria, R., and Pingol, A., “Simulating the Effects of Adsorption and Capillary Forces in Geothermal Reservoirs”, Proc. of the 21st Annual Workshop on Geothermal Reservoir Engineering, Stanford University, January 1996.

Satik, C., Ambusso, W., Castanier, L.M., and Horne, R.N., “A Preliminary Study of Relative Permeability in Geothermal Rocks”, GRC*Trans*. Vol. **19**, 1995, p. 539.

Satik, C. and Horne, R. N. (1995), “An Experimental Study of Adsorption in Vapor-Dominated Geothermal Systems”, Presented at the Twentieth Stanford geothermal Workshop 1995, Stanford, CA, Jan. 24-26.

Satik, C. and Yortsos, Y.C. (1995), “A Pore Network Model for Adsorption in Porous”, Presented at the Twentieth Stanford geothermal Workshop 1995, Stanford, CA, Jan. 24-26.

Satterfield, C.N. (1980): "*Heterogeneous Catalysis in Practice*", McGraw-Hill Book Company.

Shang, S.B., Horne, R.N., and Ramey, H.J. Jr., “Experimental Study of Water Adsorption On Geysers Reservoir Rocks”, Proc. of the 18th Annual Workshop on Geothermal Reservoir Engineering, Stanford University, California, January 1993.

Shang, S.B., Horne, R.N., and Ramey, H.J., Jr. (1994): "Measurement of Surface Area and Water Adsorption Capacity of Geothermal Reservoir Rocks",*Transactions*, Geothermal Resources Council, vol. 18.

Shang, S. B. and Horne, R. N. and Ramey, H. J., Jr. (1995) “Water Adsorption on Geothermal Reservoir Rocks”, *Geothermics* 24(4), 523-540.

Shook, M., “Generalization of Vapor Pressure Lowering Effects in an Existing Geothermal Simulator”, Idaho National Engineering Laboratory Report, Idaho, June 1993.

Shook, M., “Effects of Adsorption on Exploitation of Geothermal Reservoirs”, Geothermal Resource Council *Transactions*, Vol. 18, October 1994.

Sorey, M.L. Grant M.A. and Bradford E., “Nonlinear Effects in Two Phase Flow to Wells in Geothermal Reservoirs”, *Water Resources Research*, Vol. **16** No. 4, 1980, pp 767-777.

Sternfeld, J.N. (1989), “Lithologic Influences on Fracture Permeability and the Distribution of Steam in the Northwest Geysers Geothermal Field, Sonoma County, CA”, Geothermal Resources Council Transactions, Vol. **13**, pp. 473-479.

Thomas, R.P., Chapman, R.H., Dykstra, H. and Stockton, A.D. (1981), "A Reservoir Assessment of the Geysers Geothermal Field, CA", Div. of Mines and Geology Publication TR27, 60p.

Thompson, R.C. (1992), "Structural Stratigraphy and Intrusive Rocks at The Geysers Geothermal Field", in: Monograph on The Geysers Geothermal Field, Geothermal Resources Council, Special Report 17, pp. 59-63.

Udell, K.S. "The Thermodynamics of Evaporation and Condensation in Porous Media", SPE Paper 10779, presented at the 1982 SPE California Regional Meeting San Francisco, CA.

Verma, M.A., Pruess, K. and Witherspoon, P.A., "An Experimental Investigation of Two-Phase Steam/Water Relative Permeability in Unconsolidated Porous Medium", *Earth Science* (Berkeley California): Vol. **8**, 1985, 5-8.

Verma, M.A., "Effects of Phase Transformation of Steam-Water Two-Phase Relative-Permeability", Ph.D. Thesis, University of California, Berkeley,1986.

Walters, M.A., Sternfeld, J.N., Haizlip, J.R., Drenick, A.F., and Combs, J.B. (1988), "A Vapor-Dominated Reservoir Exceeding 600°F at The Geysers, Sonoma County, CA", Proceedings of the Thirteenth Workshop on Geothermal Reservoir Engineering, Stanford University, pp. 73-81.

White, D.E. (1973): "Characteristics of Geothermal Resources",*Geothermal Energy*, Kruger and Otte (Editors), Stanford Press, Ch.4, p. 69.